Received: 24 November 2020 | Revised: 27 February 2021 | Accepted: 28 February 2021

DOI: 10.1002/fld.4980

RESEARCH ARTICLE

WILEY

Natural convection and entropy generation in square and skew cavities due to large temperature differences: A Gay–Lussac-type vorticity stream-function approach

Peyman Mayeli | **Gregory J. Sheard**

Department of Mechanical and Aerospace Engineering, Monash University, Melbourne, Victoria, Australia

Correspondence
Peyman Mayeli, Department of Mechanical and Aerospace Engineering, Monash University, Melbourne, Vic 3800, Australia.
Email: peyman.mayeli@monash.edu

Funding information
Pawsey Supercomputing Centre through NCMAS; National Computational Infrastructure (NCI); Monash International Postgraduate Research Scholarship; Monash Graduate Scholarship; Australian Research Council through Discovery Projects, Grant/Award Numbers: DP180102647, DP150102920

Abstract

In this study, a benchmark natural convection problem is studied under a Gay–Lussac-type approximation incorporating centrifugal effects in the context of a new vorticity-stream-function approach. This approximation differs from the classic Boussinesq approximation in that density variations are considered in the advection term as well as the gravity term in the momentum equations. Such a treatment invokes Froude number as a non-Boussinesq parameter deviating results from the classic Boussinesq approximation. It is also shown how the Gay–Lussac parameter may be expressed by its equivalent relative temperature difference. Numerical simulation of natural convection in square and skewed cavities are performed up to $Ra = 10^6$ and $\varepsilon = 0.3$ at $Pr = 0.71$. Results obtained with new approximation are compared against the weakly compressible approach and the conventional Boussinesq approximation in terms of the average and local Nusselt number, coefficient of friction and entropy generation. Comparing the local Nusselt number indicates a negligible difference between Gay–Lussac type and the Boussinesq approximations even at a high relative temperature difference, with both deviating from the weakly compressible approach. Comparing coefficient friction results obtained by the Gay–Lussac-type approximation against the weakly compressible approach confirms superior numerical data in some regions of the physical domain with less deviation for rotating flows in comparison with the Boussinesq approximation. Finally, comparing the computational cost of the numerical simulation shows at least 8% less computational cost when governing equations are solved via secondary variables using a central scheme rather than primitive variables.

KEYWORDS

Gay–Lussac approximation, non-Boussinesq approximation, rotating flows, vorticity stream-function, weakly compressible approach

1 | INTRODUCTION

Traditionally, the Boussinesq approximation[1] is adopted for the numerical simulation of the natural convection problems. The simplicity of ignoring density variations except in buoyancy term and treating the flow field as incompressible while its existence is due to density variations makes the classic Boussinesq approximation popular.[2-15] Another advantage of the Boussinesq approximation that justifies its application for a broad range of the natural convection simulations is its simple implementation and accuracy of performance for problems having small temperature differences. The Boussinesq approximation, accompanied by a linear relation between density and temperature via a volumetric thermal expansion coefficient, is the basis of many numerical simulations of natural convection benchmark problems such as rectangular,[2-7] triangular[8-11] and annular[12-14] enclosed geometries.

The classic Boussinesq approximation is established based on a fundamental assumption of small density variations. Indeed, the Boussinesq approximation yields accurate results while density variations are small, whereas applying the Boussinesq approximation on cases that are featuring large density variations produces inaccurate results.[15] Such a situation may take place in foundry processes, astrophysical magnetohydrodynamic simulations[16] or solar collector systems.[17] Numerical techniques that seek to circumvent the limitations of the Boussinesq approximation are less abundant in the literature. Generally speaking, two classes of remedy are proposed to avoid the Boussinesq approximation for numerical simulation of the natural convection problems.

The first class of approaches applies the concept of compressibility that leads to introduction of the Mach number and fully compressible treatment of the Navier–Stokes equations, including acoustic waves. This strategy is seldom used for natural convection simulations due to instability caused by the small order of the compressibility ratio for density-based compressible flow solvers; examples include Vierendeels et al.,[18] Fu et al.,[19] Busto et al.,[20] and Bermúdez et al..[21] Since the order of compressibility in the natural convection problems is small, numerical simulations in this area are confined to small Mach numbers. This motivated the use of the low Mach number scheme (LMS) or weakly compressible approach. Under the LMS approximation developed by Paulucci,[22] acoustic waves are removed from the governing equation and total pressure is split into two main parts; a global (uniform) thermodynamic pressure which is obtained from the equation of state and used for updating the density variations through the solution procedure, and a local pressure which acts in the momentum equations to establish a balance among advection, buoyancy and diffusion terms. Vierendeels et al.[23] and Becker and Braack[24] employed this technique for numerical simulation of the square cavity benchmark problem with large temperature differences beyond the validity of the Boussinesq approximation.

The second class of approaches are developed in the context of the incompressible treatment of the governing equations. One such strategy is the Gay–Lussac approach, which is developed based on retaining density variations wherever density appears in the governing equations, that is, continuity and the advection/convection terms of the momentum and energy equations, respectively. Such a treatment leads to the introduction of the Gay–Lussac parameter as a product of the volumetric thermal expansion coefficient and the reference temperature difference ($\mathrm{Ga} = \beta\Delta\theta$). Under the Gay–Lussac approach, a prefactor of $(1 - \mathrm{Ga}\Theta)$ acts as a modifier on the aforementioned terms in the governing equations. The strength of this prefactor and its modification effect becomes stronger by increasing the temperature differences and consequently the Gay–Lussac parameter. It can be also shown that the Boussinesq approximation is recovered as $\mathrm{Ga} \to 0$. Pesso and Piva[25] used this strategy for the square cavity benchmark problem with large density variations. Recently, a Gay–Lussac-type approach was proposed by Lopez et al.[26] for the treatment of rapidly rotating flows, in which density variations were extended only to the centrifugal part of the advection term to capture centrifugal effects arising from background rotation in those rapidly rotating flows. Mayeli and Sheard[27] continued this approach and showed that the Gay–Lussac number may be expressed in terms of Rayleigh, Prandtl, and Froude numbers ($\mathrm{Ga} = \mathrm{RaPrFr}$) with a maximum $\mathrm{Ga}_{\max} = 2$ required to avoid an unphysical (negative) density value. Such a constraint confines the maximum physical value of the Froude number at each Rayleigh and Prandtl number to $2/\mathrm{RaPr}$ ($\mathrm{Fr}_{\max} = 2/\mathrm{RaPr}$). The study established a relation for the Gay–Lussac approach between the Froude number and the corresponding relative temperature difference (ϵ) at each Ra and Pr as $\mathrm{Fr} = 2\epsilon/\mathrm{RaPr}$.

Another incompressible-based strategy to go beyond the Boussinesq approximation is considering nonlinear terms via retention of higher terms (e.g., square and cubic terms) of the density state relation, thus extending the applicable temperature-range. Another justification of applying nonlinear density state relation comes from strange behavior of some fluids like water at temperatures close or equal to the temperature of maximum density. In this situation, the linear density state relation may not be valid anymore even for small temperature differences. For instance, the density–temperature relationship of cool water in the vicinity of 4°C does not obey a linear function. This strategy was used by Osorio et al.[28] for natural convection of water near its density inversion in an inclined square cavity.

In the Boussinesq approximation, properties of the working fluid are treated as constants, so the idea of applying variable properties (often as a function of temperature) is considered as a separate class of approximations beyond the Boussinesq approximation. However, in this approach, fundamentals of the original Boussinesq approximation are still applied. Many works have been conducted comparing this approach to the standard constant-property Boussinesq approximation. Souza et al.[29] is one example, in which all properties of the working fluid including viscosity, thermal conductivity, and heat capacity were varied as functions of temperature in a square cavity benchmark problem. They found that thermal conductivity and dynamic viscosity are the properties most sensitive to temperature variations.

In this paper, the approach of Lopez et al.[26] is adapted to a secondary-variables vorticity stream-function formulation, which is then applied to the square cavity problem. Skewed cavities are also considered for the stronger local rotations that may be invoked in the tighter corner regions. For comparison, this approximation is compared to simulations under the LMS and Boussinesq approximations, and results are compared in terms of the local and average Nusselt number, coefficient friction and entropy generation. The rest of the paper is organized as follows: Section 2 presents the aforementioned Gay–Lussac-type formulation and the LMS approximation, Section 3 introduces the geometry and boundary conditions of the problem and numerical considerations including accuracy and mesh dependency. Section 4 compares the results obtained using the three approximations, and conclusions are drawn in Section 5.

2 | GOVERNING EQUATIONS

Under the Boussinesq approximation,[1] density variations are ignored except with in the gravity term. As mentioned before, this leads to inaccurate results for problems with large density differences.[15] As mentioned earlier, a Gay–Lussac-type approach is possible through extension of density variations to the advection term of the momentum equations. In Lopez et al.,[26] the density comprises a constant (ρ_0) and a perturbation part (ρ') that captures the temperature dependences, density variations due to fluid density stratification or density variations in a binary fluid with miscible species of different densities and etc ($\rho = \rho_0 + \rho'$). Extending this decomposition from the gravity term to the full advection term produces the modified governing momentum equation in the inertial frame for a Newtonian fluid,

$$\rho_0(\partial_t + \boldsymbol{u}\cdot\nabla)\boldsymbol{u} = -\nabla p^* + \mu\nabla^2\boldsymbol{u} + \rho\boldsymbol{f} - \rho'\nabla\phi - \rho'(\boldsymbol{u}\cdot\nabla)\boldsymbol{u}. \tag{1}$$

In Equation (1), p^* is modified pressure defined as $p^* = p + \rho_0\phi$, where ϕ is the gravitational potential whose gradient opposes the gravitational acceleration vector, that is, $\nabla\phi = -g\boldsymbol{e}_g$, where $\boldsymbol{e}_g$ is the unit vector in the direction of gravity ($\boldsymbol{e}_g = \boldsymbol{g}/|\boldsymbol{g}|$). In addition, the term $\rho\boldsymbol{f}$ in Equation (1) accounts for additional body forces that may act on the fluid. Mayeli and Sheard[27] applied the same concept on the momentum equation but they used a unified definition for density. The dimensional form of the steady-state momentum equation divided by a reference density (ρ_0) in the absence of any additional body force is expressed as follows

$$(\rho/\rho_0)(\boldsymbol{u}\cdot\nabla)\boldsymbol{u} = -\frac{1}{\rho_0}\nabla p^* + \nu\nabla^2\boldsymbol{u} + (\rho/\rho_0)g\boldsymbol{e}_g. \tag{2}$$

Under the considered Gay–Lussac-type approximation, density variations are extended to the advection terms as well as gravity term. Using a linear density state equation ($\rho/\rho_0 = 1 - \beta\theta$) derived from volumetric thermal expansion coefficient definition, the momentum equation may be rewritten as follows,

$$(\boldsymbol{u}\cdot\nabla)\boldsymbol{u} = -\frac{1}{\rho_0}\nabla p^* + \nu\nabla^2\boldsymbol{u} - \beta\theta g\boldsymbol{e}_g + \beta\theta(\boldsymbol{u}\cdot\nabla)\boldsymbol{u}. \tag{3}$$

In Equation (3), a modified pressure is used which is defined as $p^* = p + \rho_0\phi$, where ϕ is the gravitational potential whose gradient opposes the gravitational acceleration vector, that is, $\nabla\phi = -g\boldsymbol{e}_g$, where $\boldsymbol{e}_g$ is the unit vector in the direction of gravity ($\boldsymbol{e}_g = \boldsymbol{g}/|\boldsymbol{g}|$). Using dimensionless quantities

$$\boldsymbol{X} = \frac{\boldsymbol{x}}{L_{\text{ref}}}, \boldsymbol{U} = \frac{\boldsymbol{u}L_{\text{ref}}}{\alpha}, P = \frac{p^*{L_{\text{ref}}}^2}{\rho_0\alpha^2}, \Theta = \frac{\theta}{\Delta\theta} = \frac{T - T_0}{T_h - T_c}, \tag{4}$$

one can derive the dimensionless form of the momentum equation for natural convection problems as follows.[25]

$$(\boldsymbol{U}\cdot\nabla)\boldsymbol{U} = -\nabla P + Pr\nabla^2\boldsymbol{U} - \mathrm{RaPr}\Theta\boldsymbol{e}_g + Ga\Theta(\boldsymbol{U}\cdot\nabla)\boldsymbol{U}. \tag{5}$$

Equation (5) introduces the Prandtl number $\mathrm{Pr} = \nu/\alpha$ characterizing the ratio of the molecular to thermal dissipation, the Rayleigh number $\mathrm{Ra} = g\beta\Delta\theta L_{\mathrm{ref}}{}^3/\nu\alpha$ characterizing the ratio of buoyancy to viscous and thermal dissipation and Gay–Lussac parameter $\mathrm{Ga} = \beta\Delta\theta$. As later be shown, the Gay–Lussac parameter may be expressed as a product of Rayleigh, Prandtl and Froude numbers, that is, Ga = FrRaPr. Thus, under this Gay–Lussac-type approximation, the dimensionless form of the governing equations in the context of the primitive variables are expressed as.[27]

$$\begin{cases} \nabla\cdot\boldsymbol{U} = 0, \\ (\boldsymbol{U}\cdot\nabla)\boldsymbol{U} = -\nabla P + Pr\nabla^2\boldsymbol{U} - \mathrm{RaPr}\Theta(\,\boldsymbol{e_g} - Fr(\boldsymbol{U}\cdot\nabla)\boldsymbol{U}), \\ (\boldsymbol{U}\cdot\nabla)\Theta = \nabla^2\Theta. \end{cases} \tag{6}$$

Equation (6) introduces Froude number $\mathrm{Fr} = U_{\mathrm{ref}}{}^2/gL$ characterizing ratio of inertial to gravitational forces. Interested readers are referred to Reference 27 for a detailed procedure of the momentum equation derivation. As can be seen, Equation (6) is consistent with the momentum equation under the Boussinesq approximation, except for the additional inertial buoyancy term on the right-hand side. When expressed in this form, it is apparent that the action of this additional term is to modify the effective direction (and strength) of the gravity locally throughout the flow which is ignored in the conventional Boussinesq approximation. Indeed, regions which are experiencing higher spatial accelerations described by $(\boldsymbol{U}\cdot\nabla)\boldsymbol{U}$, will experience deviations from the Boussinesq buoyancy approximation. The strength of these deviations relative to gravity is described by Fr, with $\mathrm{Fr}\to 0$ (and $\mathrm{Ga}\to 0$) recovering the classical Boussinesq approximation.[27] The effect of this parameter on the buoyancy-driven flow is investigated in Section 4.

Using the secondary variables, that is, vorticity ($\omega = \partial V/\partial X - \partial U/\partial Y$) and stream-function ($U = \partial\psi/\partial Y; V = -\partial\psi/\partial X$), the scalar formulation of the governing equations under mentioned Gay–Lussac-type approximation in transient form are expressed as

$$\begin{cases} \frac{\partial^2\psi}{\partial X^2} + \frac{\partial^2\psi}{\partial Y^2} = -\omega, \\ \frac{\partial\omega}{\partial t} + (1 - \mathrm{RaPrFr}\Theta)\left(\frac{\partial\psi}{\partial Y}\frac{\partial\omega}{\partial X} - \frac{\partial\psi}{\partial X}\frac{\partial\omega}{\partial Y}\right) = \mathrm{Pr}\left(\frac{\partial^2\omega}{\partial X^2} + \frac{\partial^2\omega}{\partial Y^2}\right) + \mathrm{RaPr}\frac{\partial\Theta}{\partial X}, \\ \frac{\partial\Theta}{\partial t} + \frac{\partial\psi}{\partial Y}\frac{\partial\Theta}{\partial X} - \frac{\partial\psi}{\partial X}\frac{\partial\Theta}{\partial Y} = \frac{\partial^2\Theta}{\partial X^2} + \frac{\partial^2\Theta}{\partial Y^2}, \\ \Theta(\boldsymbol{X},0) = \omega(\boldsymbol{X},0) = \psi(\boldsymbol{X},0) = 0. \end{cases} \tag{7}$$

Following the primary variables, the classical Boussinesq approximation in secondary variables are also retrieved as $Fr\to 0$.

Within this study, the square and skew-cavity cases are also simulated under the LMS approximation for comparison purpose. The dimensionless form of the governing equations under the LMS approximation are expressed as.[30]

$$\begin{cases} \frac{\partial\rho}{\partial t} + \nabla\cdot(\rho\boldsymbol{U}) = 0, \\ \frac{\partial(\rho\boldsymbol{U})}{\partial t} + \nabla\cdot(\rho\boldsymbol{U}\otimes\boldsymbol{U}) = -\nabla P + \frac{RaPr}{2\varepsilon}\rho\boldsymbol{e}_g + Pr\nabla\cdot\boldsymbol{\tau}, \\ \frac{\partial(\rho\Theta)}{\partial t} + \nabla\cdot(\rho\boldsymbol{U}\Theta) = \nabla^2\Theta + \left(\frac{\eta-1}{\eta}\right)\frac{\mathrm{d}P_{\mathrm{th}}}{\mathrm{d}t} \\ P_{\mathrm{th}} = Z\rho\Theta, \\ \Theta(\boldsymbol{X},0) = P_{\mathrm{th}}(0) = 1, \boldsymbol{U}(\boldsymbol{X},0) = 0. \end{cases} \tag{8}$$

Equation (8) has been made dimensionless using the following parameters

$$t = \frac{t^*\alpha}{L^2}, \boldsymbol{X} = \frac{\boldsymbol{x}}{L}, \boldsymbol{U} = \frac{\boldsymbol{u}L}{\alpha}, P = \frac{p^*L^2}{\rho\alpha^2}, \Theta = \frac{T}{T_0}, P_{\mathrm{th}} = \frac{p_{\mathrm{th}}}{p_0}, Z = \frac{R}{R_0}, \rho = \frac{\rho^*}{\rho_0}. \tag{9}$$

In Equation (8), Pr is the Prandtl number as defined earlier in Equation (5), ε is the relative temperature difference defined as $\varepsilon = (T_h - T_c)/2T_0$, η is the heat capacity ratio ($\eta = c_p/c_v$) and P_{th} is the global dimensionless thermodynamic pressure.

In this study, we only present results for an ideal diatomic gas ($Z = 1$). Also, $\boldsymbol{\tau}$ is the stress tensor given in dimensionless form by

$$\boldsymbol{\tau} = \nabla \boldsymbol{U} + (\nabla \boldsymbol{U})^T - 2/3(\nabla \cdot \boldsymbol{U})\boldsymbol{I}. \tag{10}$$

In Equation (9), Stokes' hypothesis is used for bulk viscosity ($\lambda = -2/3\mu$). In natural convection simulation via compressible/weakly compressible approach, the Rayleigh number is expressed slightly different compared to the incompressible flow, as

$$\mathrm{Ra} = \mathrm{Pr}\,\frac{g{\rho_0}^2(T_\mathrm{h} - T_\mathrm{c})L^3}{T_o{\mu_0}^2}. \tag{11}$$

Comparing incompressible and compressible Rayleigh number definitions gives the following relation for the Froude number corresponding to a given relative temperature difference at each Rayleigh and Prandtl as.[27]

$$\underbrace{2\varepsilon = (T_\mathrm{h} - T_\mathrm{c})/T_o}_{\text{Compressible}} = \underbrace{\beta\Delta\theta = \mathrm{RaPrFr}}_{\text{Incompressible}} \rightarrow \mathrm{Fr} = 2\varepsilon/\mathrm{RaPr}. \tag{12}$$

Another advantage of Equation (11) is expressing the Gay–Lussac parameter by its equivalent relative temperature difference definition ($2\varepsilon = \beta\Delta\theta = \mathrm{Ga}$). So, another form of the Gay–Lussac-type approach may be expressed using ε instead of Ga and/or three dominant dimensionless parameters, that is, Ra, Pr, and Fr as

$$\begin{cases} \frac{\partial^2\psi}{\partial X^2} + \frac{\partial^2\psi}{\partial Y^2} = -\omega \\ \frac{\partial\omega}{\partial t} + (1 - 2\varepsilon\Theta)\left(\frac{\partial\psi}{\partial Y}\frac{\partial\omega}{\partial X} - \frac{\partial\psi}{\partial X}\frac{\partial\omega}{\partial Y}\right) = \mathrm{Pr}\left(\frac{\partial^2\omega}{\partial X^2} + \frac{\partial^2\omega}{\partial Y^2}\right) + \mathrm{RaPr}\frac{\partial\Theta}{\partial X}, \\ \frac{\partial\Theta}{\partial t} + \frac{\partial\psi}{\partial Y}\frac{\partial\Theta}{\partial X} - \frac{\partial\psi}{\partial X}\frac{\partial\Theta}{\partial Y} = \frac{\partial^2\Theta}{\partial X^2} + \frac{\partial^2\Theta}{\partial Y^2} \\ \Theta(\boldsymbol{X}, 0) = \omega(\boldsymbol{X}, 0) = \psi(\boldsymbol{X}, 0) = 0. \end{cases} \tag{13}$$

3 | DESCRIPTION OF THE PROBLEM AND NUMERICAL APPROACH

The square and skew cavity configurations are shown in Figure 1, highlighting the thermal boundary conditions comprising adiabatic top and bottom boundaries, and hot and cold left and right boundaries, respectively. The applied boundary conditions for vorticity and stream-function are also shown. In this study, the reference length is taken to be equal to the length of the horizontal side of the geometry ($L_\mathrm{ref} = L$). Skew cavities are also defined by an skewness angle of δ. The physical domain is meshed using quadrilateral elements. A schematic coarse mesh is shown for illustration purposes in Figure 1(C),(D).

The local and average Nusselt number along the two constant temperature surfaces are calculated as

$$Nu_\mathrm{loc}(S) = -\left.\frac{\partial\Theta}{\partial n}\right|_\mathrm{wall}, \tag{14}$$

$$Nu_\mathrm{avg} = \int_0^1 Nu_\mathrm{loc}\,\mathrm{d}S. \tag{15}$$

The dimensionless local entropy generation due to heat transfer (S_θ) and fluid friction (S_ψ) are calculated as

$$S_\Theta = \left[\left(\frac{\partial\Theta}{\partial X}\right)^2 + \left(\frac{\partial\Theta}{\partial Y}\right)^2\right], \tag{16}$$

$$S_\psi = \chi\left[2\left\{\left(\frac{\partial U}{\partial X}\right)^2 + \left(\frac{\partial V}{\partial Y}\right)^2\right\} + \left(\frac{\partial U}{\partial Y} + \frac{\partial V}{\partial X}\right)^2\right]. \tag{17}$$

For compressible approach in which$\nabla \cdot \boldsymbol{U} \neq 0$, S_ψ retains the velocity divergence and must be calculated using

$$S_\psi = \chi\left[2\left\{\left(\frac{\partial U}{\partial X}\right)^2 + \left(\frac{\partial V}{\partial Y}\right)^2\right\} + \left(\frac{\partial U}{\partial Y} + \frac{\partial V}{\partial X}\right)^2 - \frac{2}{3}\left(\frac{\partial U}{\partial X} + \frac{\partial V}{\partial Y}\right)^2\right]. \tag{18}$$

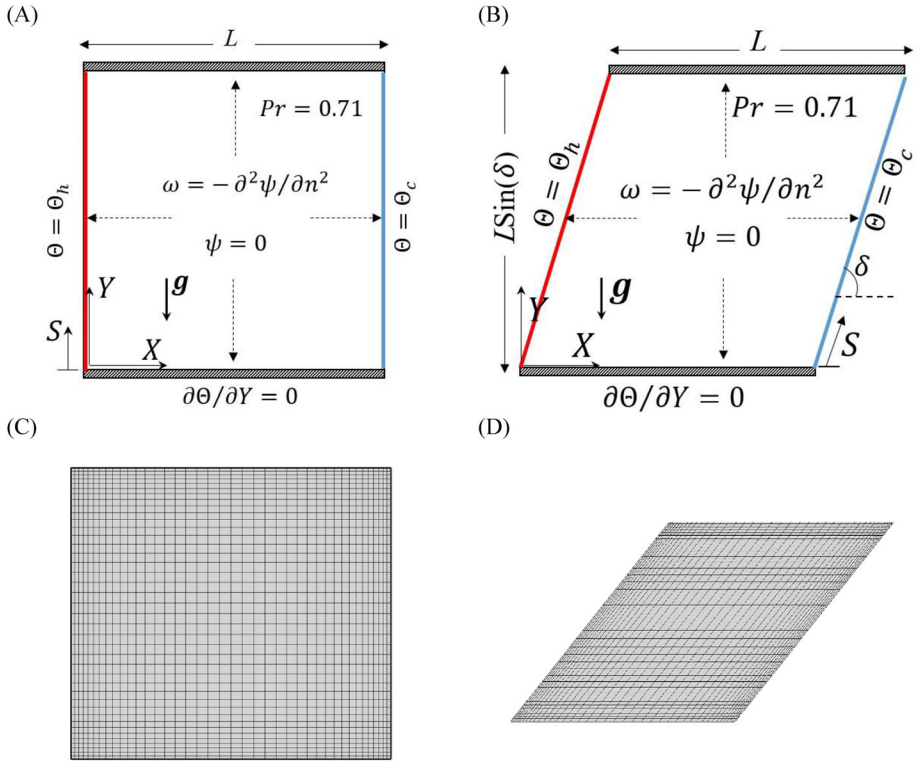

FIGURE 1 A schematic view of the problem, applied boundary conditions and used mesh, (A), Square cavity, (B), Skew cavity with skewness angle δ, (C, D), A coarse computational grid having 40×40 quadrilateral elements [Color figure can be viewed at wileyonlinelibrary.com]

In Equations (16) and (17), $\chi = \mu T_0 \alpha^2 / k(L\Delta\theta)^2$ is the irreversibility distribution ratio such that characterizes the ratio of viscous heat dissipation to heat conduction within the system. In this study, χ is taken as fixed and equal to 10^{-4} consistent with References 31–33. For context, in air at standard conditions, this corresponds to a reference length $L \sim 10^{-1}$ m and temperature difference $\Delta\theta \sim 1$ K. The total entropy generation due to heat transfer and fluid friction is calculated by the summation of the local entropy generation over the physical domain via

$$S_{\Theta,\text{tot}} = \int_V S_\Theta \, \mathrm{d}v, \tag{19}$$

$$S_{\psi,tot} = \int_V S_\psi \, \mathrm{d}v. \tag{20}$$

The relative dominance of entropy generation due to heat transfer and fluid friction is given by average Bejan number (Be_{avg}), a dimensionless parameter defined as.[34-36]

$$\text{Be}_{\text{avg}} = \frac{S_{\Theta,\text{tot}}}{S_{\Theta,\text{tot}} + S_{\psi,\text{tot}}}, \tag{21}$$

where $\text{Be}_{\text{avg}} > 0.5$ implies dominance of heat transfer irreversibility and $\text{Be}_{\text{avg}} < 0.5$ implies dominance of fluid friction irreversibility.

The skin friction along the surfaces is related to the fluid flow via the gradient of the velocity components normal to the surface. The friction coefficient along the surface based on the dimensionless velocity is defined as

$$c_f = -\frac{\tau_w}{1/2\rho(\alpha/L)^2} = -2\,\text{Pr}\,\frac{\partial U_\delta}{\partial \boldsymbol{n}}\bigg|_{\text{wall}}. \tag{22}$$

In Equation (22), $\boldsymbol{n}$ is the unit normal vector to the surface. Since the governing equations are solved in a Cartesian coordinate system, the above fundamental definition is implemented through the two-dimensional (2D) shear stress tensor as

$$\boldsymbol{c_f} = -2\,\text{Pr}\begin{bmatrix}\tau_{xx} & \tau_{xy}\\ \tau_{yx} & \tau_{yy}\end{bmatrix}\begin{bmatrix}n_x\\ n_y\end{bmatrix} = -2Pr\begin{bmatrix}2\partial U/\partial X & \partial U/\partial Y + \partial V/\partial X\\ \partial U/\partial Y + \partial V/\partial X & 2\partial V/\partial Y\end{bmatrix}\begin{bmatrix}n_x\\ n_y\end{bmatrix}, \tag{23}$$

where n_x and n_y are the horizontal and vertical components of the wall-normal vector, respectively. The friction coefficient magnitude is calculated as

$$c_f = \sqrt{(c_{f_x})^2 + (c_{f_y})^2}, \tag{24}$$

where

$$c_{f_x} = -2\,\mathrm{Pr}[(2\partial U/\partial X)n_x + (\partial U/\partial Y + \partial V/\partial X)n_y], \tag{25}$$

$$c_{f_y} = -2\,\mathrm{Pr}[(\partial U/\partial Y + \partial V/\partial X)n_x + (2\partial V/\partial Y)n_y]. \tag{26}$$

Governing equations are solved using a control volume finite-element method (CVFEM) solver with a second-order Adams Bashforth/Crank Nicolson temporal scheme for time-dependent equations having two steps. In the first step, an intermediate vorticity/temperature field is predicted using vorticity/temperature fields from the current and previous time-steps. For instance, for vorticity equation this can be shown using ω^n and ω^{n-1} as

$$\frac{\omega^* - \omega^n}{\Delta t} = -\frac{3}{2}(1 - 2\varepsilon\Theta^n)\mathrm{N}(\omega^n) + \frac{1}{2}(1 - 2\varepsilon\Theta^{n-1})\mathrm{N}(\omega^{n-1}) + \frac{Pr}{2}\mathrm{D}(\omega^n) + B^n. \tag{27}$$

In Equation (27), N and D represent the nonlinear advection and diffusion operators, respectively, and B is the buoyancy source term (i.e., $\mathrm{RaPr}\partial\Theta/\partial X$). Using intermediate vorticity (ω^*), vorticity in the next step time-step is obtained using

$$\frac{\omega^{n+1} - \omega^*}{\Delta t} = \frac{\mathrm{Pr}}{2}\mathrm{D}(\omega^{n+1}). \tag{28}$$

Equation (28) is a linear equation that is solved implicitly to update the vorticity field in each iteration. A similar procedure is applied for the energy equation to update the temperature field during iterations.

In CVFEM, a unique control volume (as shown in Figure 2(A)) is assigned to each node that its boundaries are comprised of a number of planar panels. An integration point (ip) is located at the middle of each panel, which is denoted by a × sign. Integration of diffusion term over the control volume and applying the Gauss divergence theorem yields

$$\int_{v_p} \nabla^2\omega \mathrm{d}v = \oint_{A_p} \nabla\omega_{\mathrm{ip}} \cdot \mathrm{d}\boldsymbol{A} = \sum_{\mathrm{ip}=1}^{n} \nabla\omega_{\mathrm{ip}} \cdot \boldsymbol{A}_{\mathrm{ip.}} \tag{29}$$

In Equation (29), n is the number of integration points surrounding the main node and $\boldsymbol{A}_{\mathrm{ip}}$ is the normal vector surface at each ip. Using bilinear shape functions ($N_j(s, t)$), any parameter (such as ω) within the element with a local coordinate (s,t) is related to the nodal values via weighted values provided by shape functions

$$\omega_{ip} = \omega(s, t) = \sum_{j=1}^{4} N_j(s, t)\omega_j. \tag{30}$$

For quadrilateral elements, the four shape functions relating *ip* values to the nodal values are shown in Figure 2(B). Thus, the diffusion term may be expressed as follows

$$D(\omega) = \sum_{\mathrm{ip}=1}^{n} \sum_{j=1}^{4} \omega_j \nabla N_j \cdot \boldsymbol{A}_{\mathrm{ip}}. \tag{31}$$

Since the bilinear shape functions are functions of their local coordinate system, their gradients with respect to global coordinate system are calculated using the chain rule. In Equation (31), the effect of all nodes surrounding an ip (such as the one shown in Figure 2(B)) are considered by weighted values that is equivalent to a central scheme. The diffusion operator in energy and stream function equations is calculated in a similar fashion.

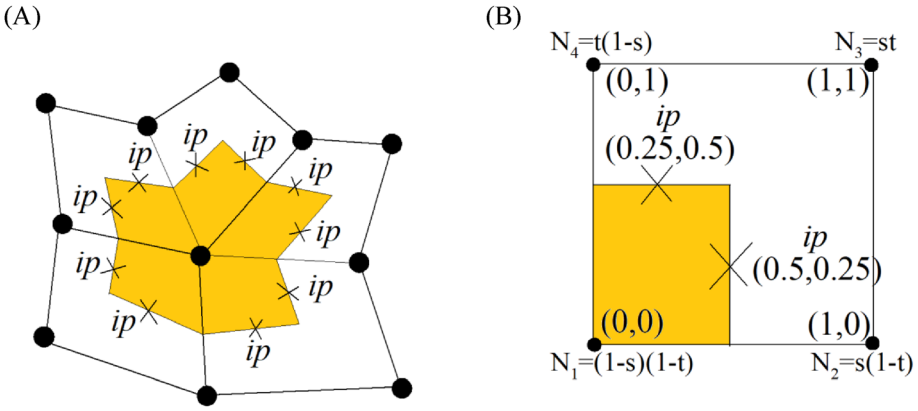

FIGURE 2 A schematic of unstructured quadrilateral elements, (A), a typical control volume associated with integration points, (B), Local coordinate (s,t) and bilinear shape functions in a standard element [Color figure can be viewed at wileyonlinelibrary.com]

	Quantity	Present study	Davis[2]	Wan et al.[6]	Ashrafizadeh and Nikfar[7]
$Ra = 10^4$	Nu_{max} (at Y)	**3.548 (0.140)**	3.53 (0.143)	3.597 (0.13)	3.531 (0.139)
	Nu_{min} (at Y)	**0.589 (1.0)**	0.586 (1.0)	0.577 (1.0)	0.584 (1.0)
	Nu_{avg}	**2.23**	2.42	2.25	2.24
$Ra = 10^5$	Nu_{max} (at Y)	**7.778 (0.075)**	7.71 (0.08)	7.945 (0.08)	7.720 (0.084)
	Nu_{min} (at Y)	**0.734 (1.0)**	0.729 (1.0)	0.698 (1.0)	0.726 (1.0)
	Nu_{avg}	**4.51**	4.52	4.60	4.52
$Ra = 10^6$	Nu_{max} (at Y)	**17.633 (0.038)**	17.92 (0.038)	17.86 (0.03)	17.732 (0.039)
	Nu_{min} (at Y)	**0.996 (1.0)**	0.989 (1.0)	0.913 (1.0)	0.975 (1.0)
	Nu_{avg}	**8.82**	8.92	8.98	8.83

TABLE 1 Comparison of the present calculated local and average Nusselt number by control volume finite-element method solver (bold) with published benchmarks

In the governing equations, non-linear terms are linearised using lagged values from the previous iteration. Integration of the advection term over the control volume and applying Gauss divergence theorem yields

$$\int_{v_p} (\overline{\psi_y}\omega_x - \overline{\psi_x}\omega_y)\mathrm{d}v = \oint_{A_p} \overline{\psi_y}\omega \mathrm{d}A_x - \overline{\psi_x}\omega \mathrm{d}A_y = \oint_{A_p} \omega(\overline{\psi_y}\mathrm{d}A_x - \overline{\psi_x}\mathrm{d}A_y) = \sum_{\mathrm{ip}=1}^{n} \omega_{\mathrm{ip}}(\overline{\psi_{y_{\mathrm{ip}}}}A_{x\mathrm{ip}} - \overline{\psi_{x_{ip}}}A_{y_{\mathrm{ip}}}). \tag{32}$$

Using bilinear shape functions (Equation (30)) to relate the integral point values to the nodal values yields

$$\mathrm{N}(\omega) = \sum_{\mathrm{ip}=1}^{n} \sum_{j=1}^{4} \omega_j N_j(\overline{\psi_{y_{\mathrm{ip}}}}A_{x\mathrm{ip}} - \overline{\psi_{x\mathrm{ip}}}A_{y_{\mathrm{ip}}}). \tag{33}$$

Similarly, in Equation (33) n is the number of ip surrounding the main node. In Equation (33), it is possible to approximate lagged values simply from the nodes within the element by weighted values (that are provided by shape functions based on local coordinate at each ip) which leads to a central scheme. Another possible scenario is approximating lagged values based on flow direction that is known as the upwind scheme. It should be noted that $\overline{\psi_{y_{\mathrm{ip}}}}$ and $-\overline{\psi_{x_{\mathrm{ip}}}}$ in vorticity and energy equations are indeed the velocity components that are expressed in the context of stream-function. The convection term in energy equation is calculated in a similar fashion. Iterative solution procedure is stopped as soon as the maximum difference of scalar values during two successive iterations becomes less than 10^{-7}. Accurate performance of the CVFEM solver is already tested in previous works[37-45] but here in Table 1 it is further validated against References 2, 6, 7 in terms of the local and average Nusselt number at three different Rayleigh numbers, adopting air as the working fluid (Pr = 0.71). A close agreement is observed.

Accurate performance of the CVFEM solver under the LMS approximation is also validated against Reference 46 in terms of average Nusselt number and thermodynamic pressure at Ra = 10^6 and ε = 0.6 with air as the working

TABLE 2 Comparison of the present calculated local and average Nusselt number by control volume finite-element method solver (bold) with published benchmarks

	Quantity	Present study	Le Quéré et al.[44]
$Ra = 10^6$, $\varepsilon = 0.6$ Constant properties	P_{th}	0.858	0.856
	Nu_{avg}	8.895	8.859
$Ra = 10^6$, $\varepsilon = 0.6$ Variable properties	P_{th}	0.921	0.924
	Nu_{avg}	8.693	8.686

TABLE 3 Mesh resolution study for average Nusselt and Bejan numbers at $Ra = 10^6$ and $Pr = 0.71$

	$n_x \times n_y$	31^2	61^2	121^2	241^2
Boussinesq approximation (Fr = 0)	Nu_{avg}	8.695134	8.811059	8.827201	8.827201
	|difference|	—	0.115925	0.016142	0.000000
	Be_{avg}	0.029368	0.026270	0.025471	0.025471
	|difference|	—	0.003098	7.99e-4	0.000000
Gay–Lussac-type approximation (Fr = 0.6/RaPr)	Nu_{avg}	8.654427	8.790351	8.816621	8.8166
	|difference|	—	0.135923	0.026270	0.000000
	Be_{avg}	0.029308	0.026222	0.025424	0.025424
	|difference|	—	0.003086	7.98e-4	0.000000

TABLE 4 Mesh resolution study for average Nusselt number and thermodynamic pressure at $Ra = 10^6$, $Pr = 0.71$, and $\varepsilon = 0.3$

	$n_x \times n_y$	31^2	61^2	121^2	241^2
LMS approximation	P_{th}	0.961124	0.964295	0.966286	0.966286
	|difference|	—	0.003171	0.001991	0.000000
	Nu_{avg}	8.992231	8.904211	8.854831	8.854831
	|difference|	—	0.088020	0.049379	0.000000

fluid ($Pr = 0.71$) in two states including constant and variable properties (see Table 2). The present simulations recover published values very well, with discrepancies lower than 0.41%.

Mesh dependence is checked for the CVFEM solver in Table 3 at the highest Rayleigh number $Ra = 10^6$ and $Pr = 0.71$ under the Boussinesq approximation ($Fr = 0$) and the highest Froude number under the Gay–Lussac-type approximation in this study ($Fr = 0.6/RaPr$). It is found that 121 nodes in each direction guarantees mesh independence for both of the Boussinesq and Gay–Lussac-type approximations.

Mesh dependence of the CVFEM solver under the LMS approximation is also checked in Table 4 at the highest Rayleigh number $Ra = 10^6$ and $Pr = 0.71$ for the highest relative temperature difference ($\varepsilon = 0.3$) in this study. It is found using 121 nodes ($n_x \times n_y = 121^2$) in each direction guarantees results independence from the mesh size for the weakly compressible approach. Similar dependence is also found for the skew cavity cases but for the sake of brevity, they are not mentioned here.

4 | RESULTS AND DISCUSSION

In this section, the results of three approximations are presented. Simulations are performed at $Pr = 0.71$ (consistent with air) up to $Ra = 10^6$ ($10 \leq Ra \leq 10^6$) and $\varepsilon = 0.3$ ($0 \leq \varepsilon \leq 0.3$). It should be noted that, a relative temperature difference of 0.01 is considered as a differential relative temperature difference and is representative of a Boussinesq case.[29] Here, we extend this parameter to 30 times larger, beyond the validity of the Boussinesq approximation. Studying relative temperature differences exceeding 0.3 is beyond the scope and goals of this paper. Based on Equation (12) and according to the

considered range of ε, Froude number ranges over $0 \leq \mathrm{Fr} \leq 0.6/\mathrm{RaPr}$ throughout this study. For the investigated range of the Froude and Rayleigh numbers at $\mathrm{Pr} = 0.71$, it is supposed that the flow field is 2D, laminar and stable.

For a better understanding of the produced thermo-flow field under the different approximations, absolute temperature differences of the weakly compressible approach at $\mathrm{Ra} = 10^6$ and $\varepsilon = 0.3$ (the highest Rayleigh number and relative temperature difference in this study) against the Gay–Lussac-type approximation with $\mathrm{Fr} = 0.6/\mathrm{RaPr}$ and the Boussinesq approximation ($\mathrm{Fr} = 0$) are depicted in Figures 3(A)–(F). Absolute temperature differences under the different approaches shift isotherms, with a larger differences found for the left-inclined skew cavity ($\delta = 150^\circ$) compared to the square cavity and right-inclined skew cavity ($\delta = 30^\circ$). In the square cavity, the difference is largest at the top-left and bottom-right corners while in the right-inclined skew cavity it is occurring almost evenly over the interior region. Large temperature differences for left-inclined skew cavities may be attributed to the reaction of accelerated fluid which is faced with an acute angle to rotate. The maximum absolute temperature difference in the square cavity in Figure 3(B),(E) (with a larger difference for the Gay–Lussac-type approximation) is approximately 10% of the temperature range within the enclosure, reflecting a mismatch of this magnitude between the weakly compressible and incompressible approaches. A similar comparison for the right-inclined skew cavity shows a smaller about 7% mismatch (Figure 3(A), (D)) while the largest mismatch of about 20% is found for the left-inclined skew cavity (Figure 3(C),(F)). It is clear that the mismatch between the aforementioned approaches augments by increasing the relative temperature difference and consequently the non-Boussinesq parameter (i.e., Froude number). To appreciate the role of extra term effects in the momentum equation of the Gay–Lussac-type approximation, the magnitude of $\Theta(\psi_y \omega_x - \psi_x \omega_y)$ under the Boussinesq approximation is portrayed for the square cavity and skew cavities with $\delta = 30^\circ$ and 150° at $\mathrm{Ra} = 10^6$ in Figures 3(G),(I). As seen, the magnitude of the non-Boussinesq acceleration is stronger along the isothermal walls and especially at four corners of the cavity, though weaker effects are found within the central regions of the enclosure. Stronger non-Boussinesq effects along the isothermal walls may be attributed to larger velocity gradients since fluid adjacent to the wall is accelerated by buoyancy force as it reaches to the wall during circulation and decelerated as it gets close to the end of the path parallel to the isotherm wall. Stronger non-Boussinesq effects at the four corners are attributed to fluid rotation to adjust its motion with respect to the geometry corners. Non-Boussinesq term magnitude is smaller for skew cavities compared to the square cavity but its magnitude is stronger in the left-inclined ($\delta = 150^\circ$) versus the right-inclined cavity ($\delta = 30^\circ$) skew cavity. Smaller magnitude of the non-Boussinesq term in skew cavities is due to a weaker thermally driven flow in skew cavity having smaller stream-function compared to square cavity as shown in the next figures (Figures 4(A), (C), 5(A), C, 6(A) and (C)).

Stream-function and vorticity absolute differences fields under the three approximations at $\mathrm{Ra} = 10^6$ and $\varepsilon = 0.3$ are portrayed for square and skew cavities with $\delta = 30^\circ$ and 150° in Figures 4, 5, and 6, respectively. In Figures 4(A), (C), 5(A), (C), 6(A) and (C), the general structure of the stream-function under the weakly compressible approach is considerably different compared to the Gay–Lussac and Boussinesq approximations in both square and skew geometries. Under the incompressible approximations, stream-functions have a twin core with almost equal strength but under the weakly compressible approximation, stream-function has one central core with a stronger circulation. In the square cavity, the location of the minimum stream-function obtained from incompressible simulations have shifted their place to a higher level toward the vertical centre-line compared to the obtained results under the weakly compressible approximation. The exact quantitative distance between the minimum stream-function locations is obtained equal to 0.1893 and 0.2048 length units for the Gay–Lussac-type and Boussinesq approximations, respectively. For the right skewed cavity with $\delta = 30^\circ$ (Figure 5), a stronger circulation is observed for the left main core under the weakly compressible approximation which is so close to the minimum stream-function location when governing equations are treated under Gay–Lussac approximation. In this case, the distances of the minimum stream-function location are obtained equal to 0.0144 and 0.2970 length units for the Gay–Lussac-type and Boussinesq approximations, respectively. Finally, a visible inclined distance is observed for left skewed cavity with $\delta = 150^\circ$ under different approximations, which is presented in Figure 6. In this case, the distances of the minimum stream-function location are obtained equal to 0.2362 and 0.2688 unit of dimensionless length for the Gay–Lussac and Boussinesq approximations, respectively. In general, obtained absolute stream-function differences show more deviation from the compressible simulation for the Gay–Lussac compared to the Boussinesq approximation with a concentration on four corners, but it predicts the minimum stream-function location more accurately than the Boussinesq approximation.

Obtained vorticity fields are presented under the different approximations in Figures 4(B), (D), 5(B), (D), 6(B) and (D). Comparing obtained results from different approaches reveals that when the buoyancy driven flow is simulated via weakly compressible approach for large relative temperature difference, the same pattern of vorticity field is formed and the difference mainly comes from vortexes (with different strengths) stretching or location shifting through the flow field.

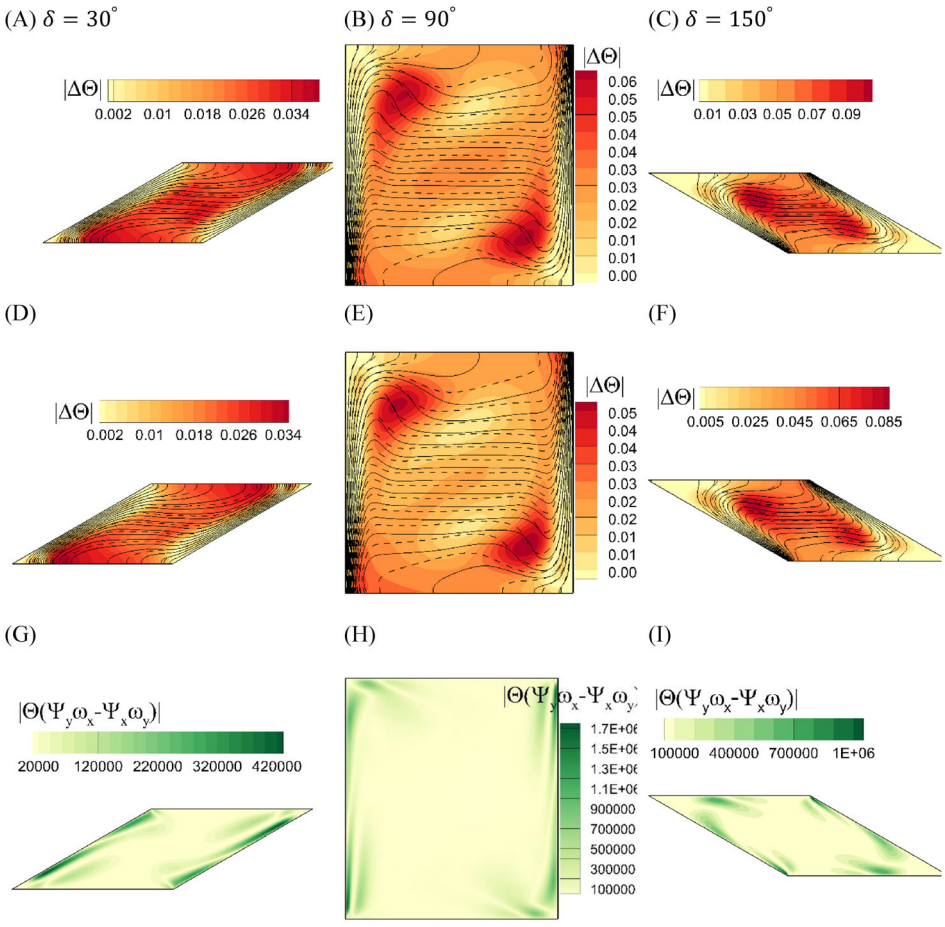

FIGURE 3 Results at $Ra = 10^6$, $Pr = 0.71$, and $\varepsilon = 0.3$, (A-C) Absolute temperature difference field between the Gay–Lussac-type and LMS approximations, (D–F) Absolute temperature difference field between the Boussinesq and LMS approximations. (G–I) Magnitude of the acceleration vector field of the non-Boussinesq acceleration term, that is, $|\Theta(\psi_y\omega_x - \psi_x\omega_y)|$ obtained from simulation under the Boussinesq approximation. In temperature difference fields, solid lines represent the LMS approximation isotherms lines at $Fr = 0.6/RaPr$ while dashed lines show the other approach [Color figure can be viewed at wileyonlinelibrary.com]

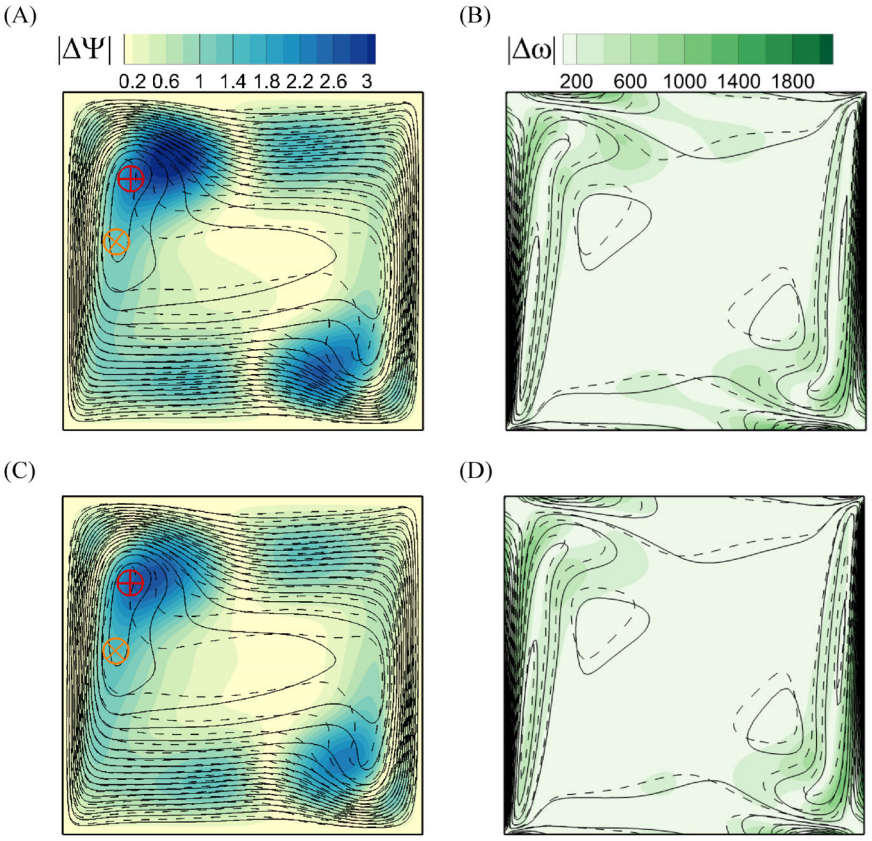

FIGURE 4 Vorticity and stream-function absolute differences in square cavity at $Ra = 10^6$ and $\varepsilon = 0.3$, (A, B) LMS and Gay–Lussac approximations, (C,D) LMS and Boussinesq approximations. "⊕" and "⊗" signs identify the point of the minimum stream-function under the LMS and incompressible approaches, respectively. In (A, C) solid and dashed lines show stream-functions under the LMS and incompressible approximations, respectively, while in (B, D) solid and dashed lines show vorticity fields under the LMS and incompressible approximations, respectively [Color figure can be viewed at wileyonlinelibrary.com]

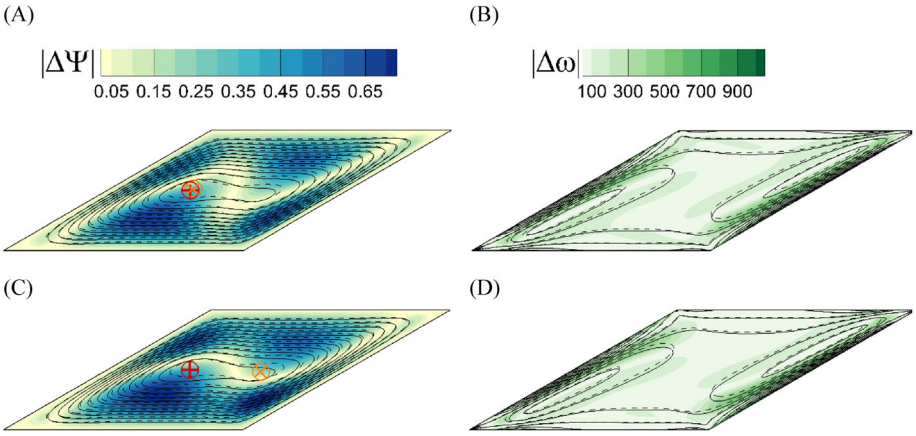

FIGURE 5 Vorticity and stream-function absolute differences in skew cavity with $\delta = 30^{\circ}$ at $\mathrm{Ra} = 10^6$ and $\varepsilon = 0.3$, (A, B), LMS and Gay–Lussac-type approximations, (C,D) LMS and Boussinesq approximations. "⊕" and "⊗" signs identify the point of the minimum stream-function under the LMS and incompressible approaches, respectively. In (A, C) solid and dashed lines show stream-functions under the LMS and incompressible approximations, respectively, while in (B, D) solid and dashed lines show vorticity fields under the LMS and incompressible approximations, respectively [Color figure can be viewed at wileyonlinelibrary.com]

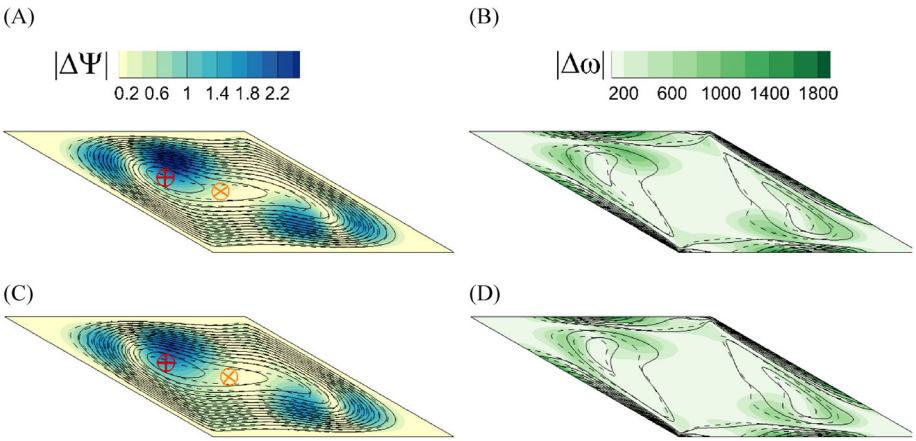

FIGURE 6 Vorticity and stream-function absolute differences in skew cavity with $\delta = 150^{\circ}$ at $\mathrm{Ra} = 10^6$ and $\varepsilon = 0.3$, (A, B) LMS and Gay–Lussac-type approximations, (C, D) LMS and Boussinesq approximations. "⊕" and "⊗" signs identify the point of the minimum stream-function under the LMS and incompressible approaches, respectively. In (A, C) solid and dashed lines show stream-functions under the LMS and incompressible approximations, respectively, while in (B, D) solid and dashed lines show vorticity fields under the LMS and incompressible approximations, respectively [Color figure can be viewed at wileyonlinelibrary.com]

In mentioned figures, large values of the vorticity absolute differences are mainly elongated adjacent to the isotherm walls where flow accelerates due to buoyancy force. For square and left skewed cavities, large values of vorticity absolute differences are also observed when accelerated rotating flow reaches to horizontal adiabatic surface.

A comparison of the temperature and velocity magnitude differences in the square cavity during transient solution is performed in Figures 7 and 8, respectively. Results of comparing transient temperature fields indicate that the Boussinesq approximation shows more deviation at the initial time of the transient solution but as the time goes on, this difference becomes less noticeable. In addition, results of the transient absolute temperature difference fields indicate that the two main cores of the temperature differences in Figure 3(B),(E) are first generated across the frontiers progressing hot and cold temperatures at the top-left and bottom right regions and then circulated in the flow direction. Comparing the values of $|\Delta\Theta|$ in steady (Figure 3) and transient (Figure 7) states reveals the absolute temperature difference between the compressible and incompressible approaches is larger in transient state compared to the steady-state solution. Comparing velocity magnitude during transient solution in Figure 8 shows a negligible difference between the Gay–Lussac type and the Boussinesq approximations against the LMS approximation. Results of the transient velocity magnitude difference

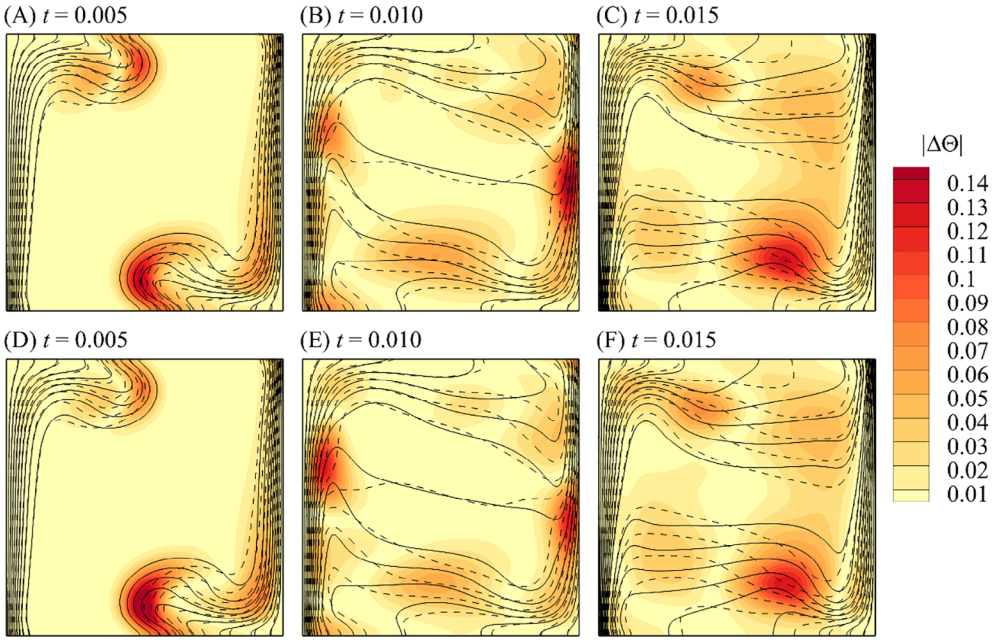

FIGURE 7 Absolute temperature difference field at different time as stated between, (A–C) The Gay–Lussac-type and LMS approximations, (D–F) The Boussinesq and LMS approximations. Solid and dashed lines show isotherms lines under the LMS and incompressible approximations, respectively [Color figure can be viewed at wileyonlinelibrary.com]

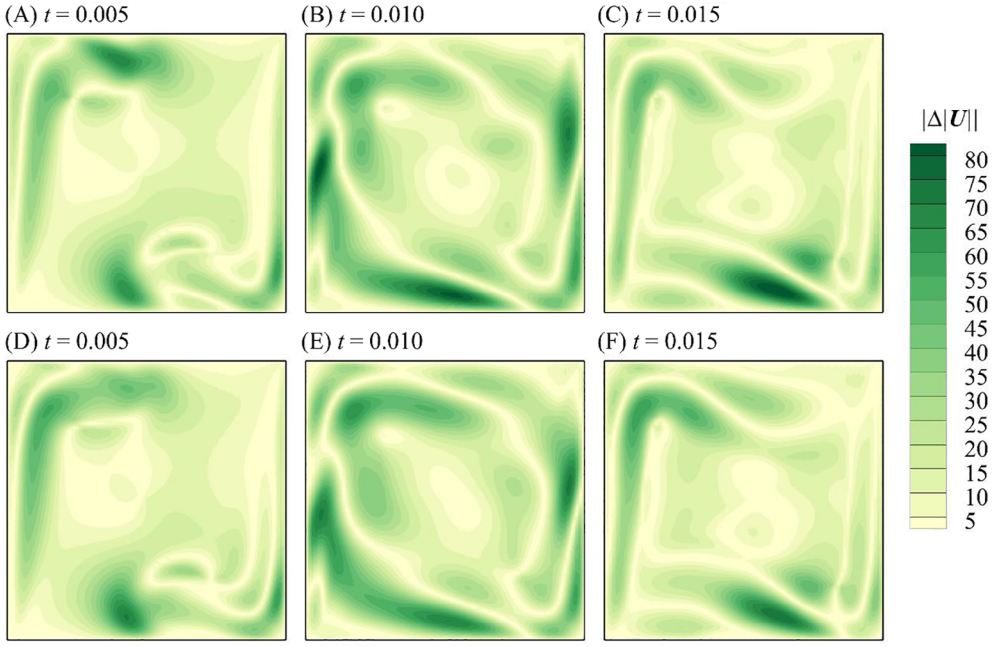

FIGURE 8 Absolute velocity magnitude difference at different time as stated between, (A–C) The Gay–Lussac-type and LMS approximations, (D–F) The Boussinesq and LMS approximations. Solid and dashed lines show isotherms lines under the LMS and incompressible approximations, respectively [Color figure can be viewed at wileyonlinelibrary.com]

indicate at the initial time of the solution (Figure 8(A),(D)), the difference mainly occurs in the regions close to the vertical walls affected by the buoyancy forces, but as the temperature field evolves toward the steady-state solution, the propagated velocity magnitude differences (Figure 8(B),(D)), concentrate mainly at the bottom-right and top-left corners (Figure 8(C),(F)).

4.1 | Local Nusselt number

The local Nusselt number distribution along the isothermal walls under the different approximations are plotted in Figure 9 at $\mathrm{Ra} = 10^6$, $\mathrm{Pr} = 0.71$, and $\varepsilon = 0.3$ for different geometries. As seen, the local Nusselt number distributions versus surface length is reversal for two isothermal walls. This may be attributed to the increasing and decreasing thermal boundary layer thickness along the isothermal walls in flow direction for the left and right walls, respectively. For

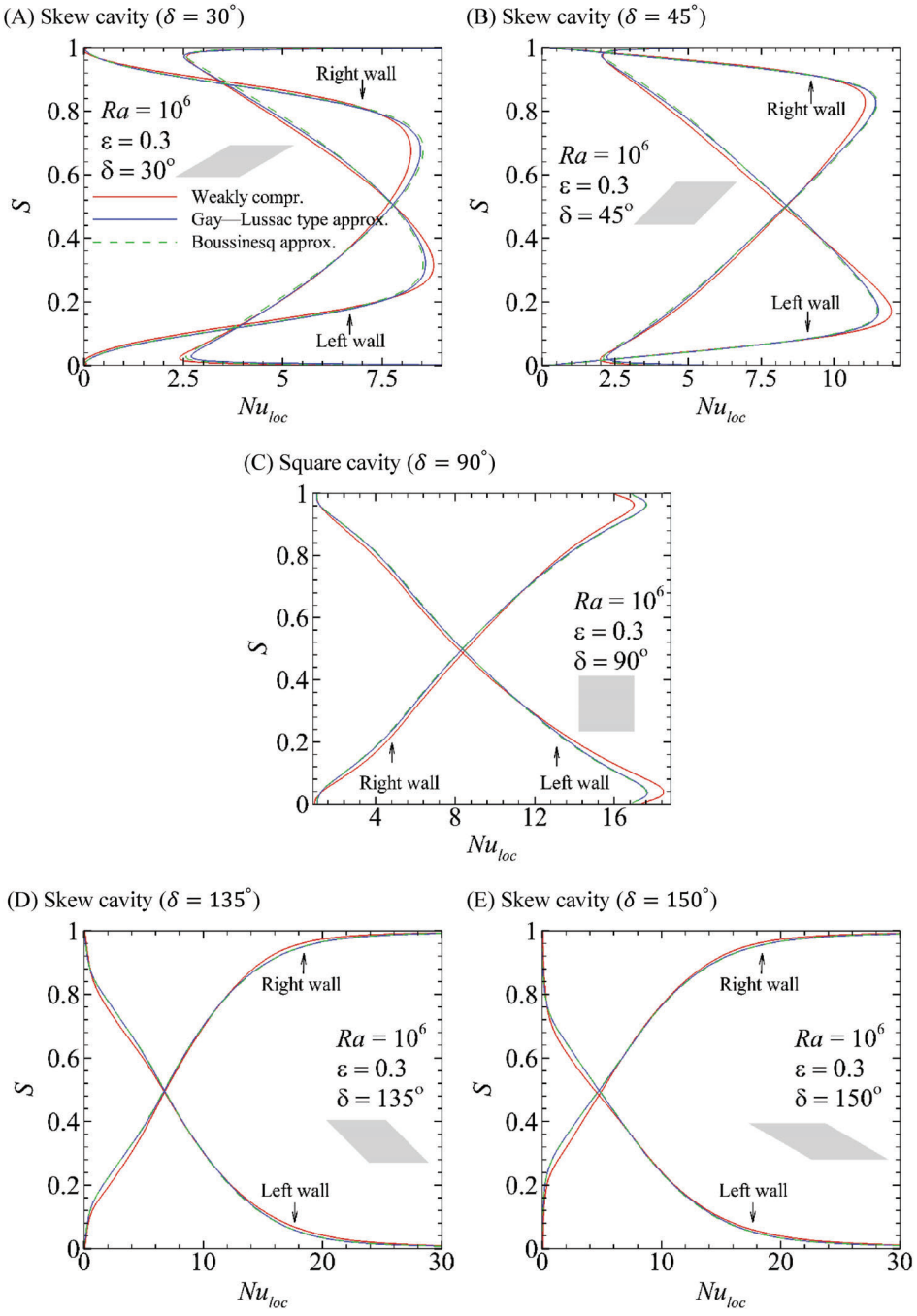

FIGURE 9 Local Nusselt number distribution along the isothermal walls at Ra = 10^6, Pr = 0.71, and $\varepsilon = 0.3$ in square and skew cavities with δ values as stated, (A) $\delta = 30^{\circ}$, (B) $\delta = 45^{\circ}$, (C) $\delta = 90^{\circ}$, (D) $\delta = 135^{\circ}$ and (E) $\delta = 150^{\circ}$ [Color figure can be viewed at wileyonlinelibrary.com]

the square cavity, there is a monotonic distribution of the local Nusselt number with a local optimum at bottom-left and top-right corners but for the right skewed cavity ($\delta = 30^{\circ}$ and 45°) this changes to a sharp oscillating behavior having smaller local Nusselt number with an optimum location at the middle height of the isothermal walls. For the left skewed cavity ($\delta = 135^{\circ}$ and 150°), there is a decreasing and increasing distribution of the local Nusselt number with no optimum location. Indeed, local Nusselt number distribution in the left-skewed cavity mimics behavior of natural convection along a vertical plate in free space. Comparing local Nusselt number distributions along the isothermal walls show a clear mismatch between incompressible and compressible approximations with slightly closer results to the compressible approach for the Gay–Lussac approximation. For the square and right skew cavities, the mismatch is more visible around the optimum location of the local Nusselt number distributions but for the left skewed cavity, the mismatch mostly occurs at the top-left and bottom-right regions. Since the difference of the local Nusselt number distributions becomes smaller by decreasing the relative temperature difference, results for the lower values of this parameter are not presented for the sake of brevity.

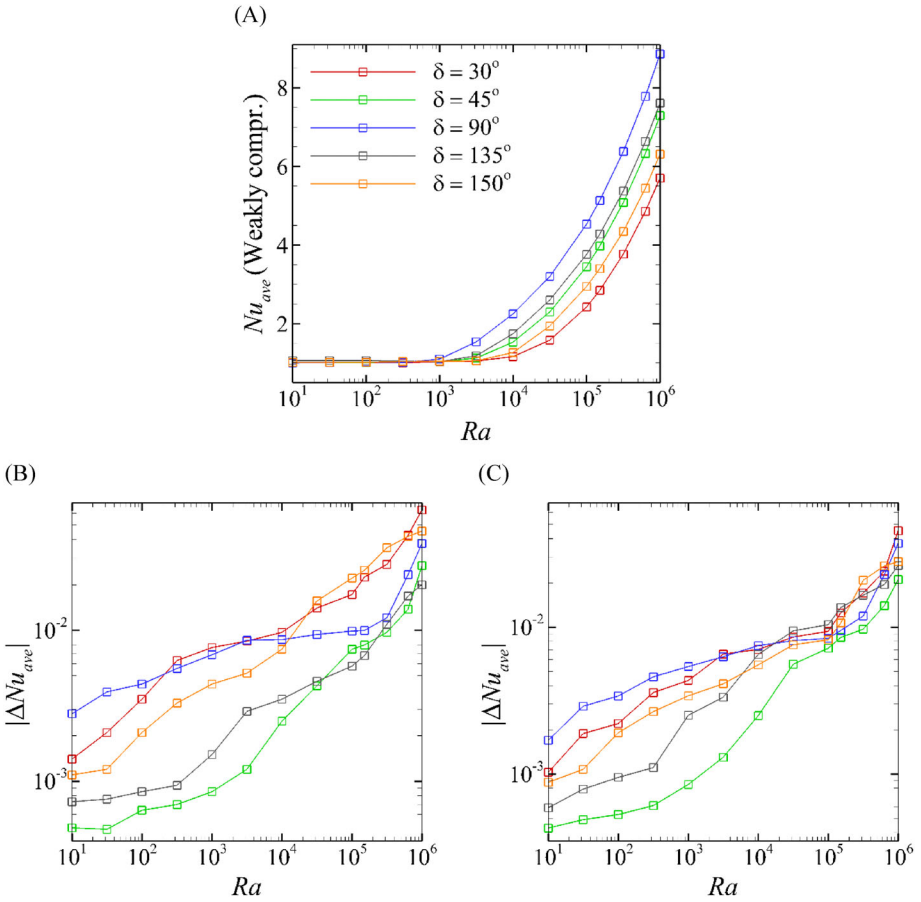

FIGURE 10 A plot of average Nusselt number against Rayleigh number at Pr = 0.71 and $\varepsilon = 0.3$ in square and skew cavities with δ values as stated, (A) Average Nusselt number for different skewness angles under the LMS approximation, (B) Absolute average Nusselt number differences between the Gay–Lussac and LMS approximations, (C) Absolute average Nusselt number differences between the Boussinesq and LMS approximations [Color figure can be viewed at wileyonlinelibrary.com]

4.2 | Average Nusselt number

The variations of the average Nusselt number across $10^1 \leq \mathrm{Ra} \leq 10^6$ is studied at the highest relative temperature difference in this study ($\varepsilon = 0.3$) under the different approximations in Figure 10. Average Nusselt number under the LMS approximation for different geometries ($\delta = 30^\circ$, 45°, 90°, 135°, and 150°) is plotted in Figure 10(A). As expected, the average Nusselt number augments by increasing the Rayleigh number. Since the values of the average Nusselt number under the different approximations are so close together, the absolute average Nusselt number differences between the LMS and two incompressible approximations are plotted in Figure 10(B),(C). Negligible differences between the average Nusselt numbers of compressible and incompressible approximations stems from opposite behavior of the local Nusselt number distributions. For instance, in square cavity problem (Figure 9(C)), the approximation that has a lower local Nusselt number distribution along $0 \leq S \leq 0.5$ has a larger value at $0.5 \leq S \leq 1$ and vice versa. This nullifies the difference of the local Nusselt number distribution and gives a small difference of the average Nusselt number for compressible and incompressible approaches. However, the total differences of the average Nusselt number for both incompressible approximations increases by increasing the Rayleigh number, but it never exceeds 10^{-1} in considered range of ε and Ra in this study. The small difference of the average Nusselt number between the Boussinesq and Gay–Lussac approximations comes from close results of the local Nusselt number distribution for this two approaches as they are almost attached together up to $\varepsilon = 0.3$ in all presented local Nusselt number distribution in Figure 9. Finally, comparing the average Nusselt number slope versus the Rayleigh number in Figure 10(A) reveals that, skewing cavity decreases the total rate heat transfer. Reduction of the average Nusselt number is more sensible for the right-skewed cavity compared to the left one.

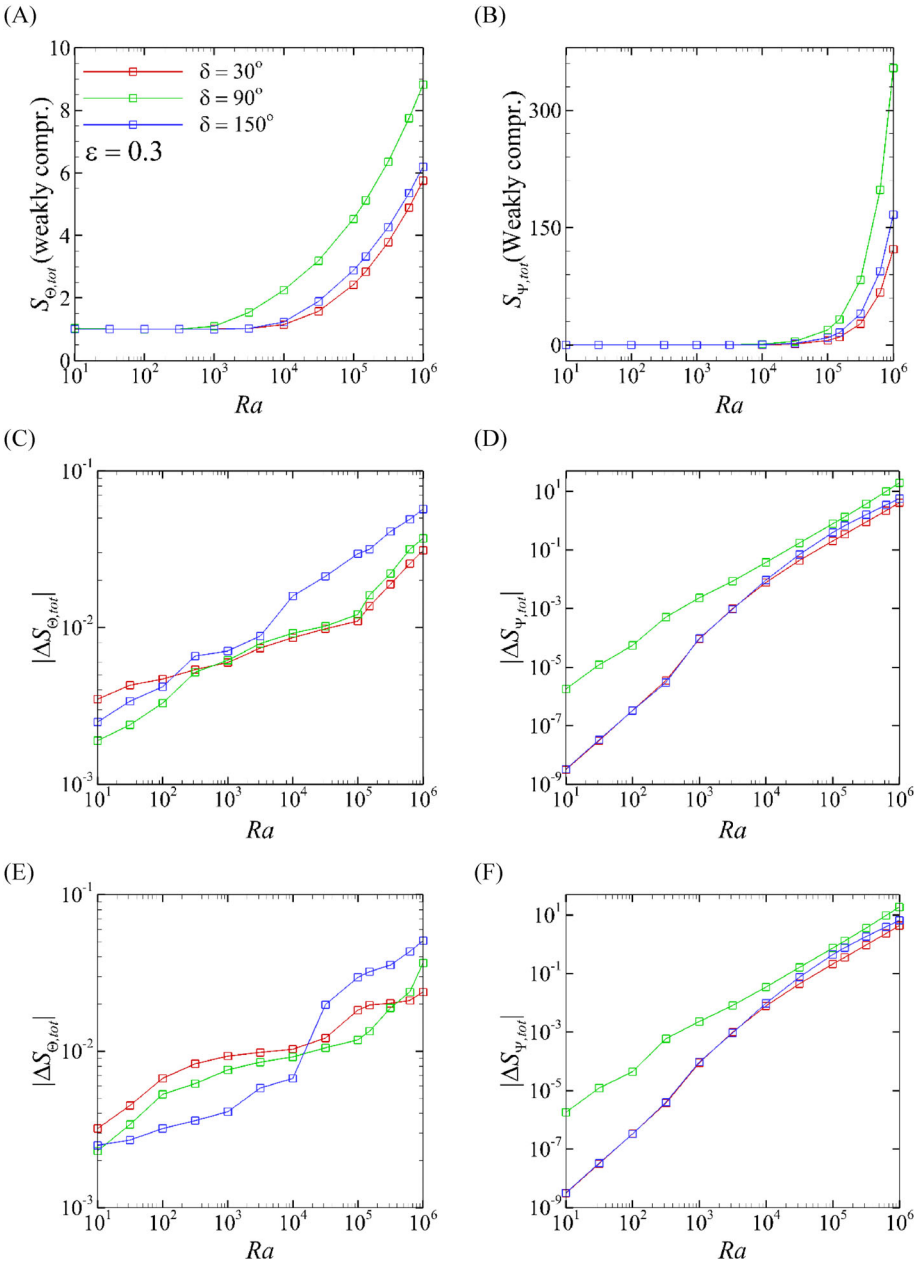

FIGURE 11 A plot of total entropy generation due to heat transfer ($S_{\Theta,\,tot}$) and fluid friction ($S_{\psi,\,tot}$) against the Rayleigh number at Pr = 0.71 and ε = 0.3, (A) $S_{\Theta,\,tot}$ under the LMS approximation at three different angles, (B) $S_{\psi,\,tot}$ under the LMS approximation at three different angles, (C) Absolute difference of $S_{\Theta,\,tot}$ between the Gay–Lussac and LMS approximations, (D) Absolute difference of $S_{\psi,\,tot}$ between the Gay–Lussac and LMS approximations, (E) Absolute difference of $S_{\Theta,\,tot}$ between the Boussinesq and LMS approximations, (F) Absolute difference of the $S_{\psi,\,tot}$ between the Boussinesq and LMS approximations [Color figure can be viewed at wileyonlinelibrary.com]

4.3 | Entropy generation

Total entropy generation due to heat transfer ($S_{\Theta,\,tot}$) and fluid friction ($S_{\psi,\,tot}$) is investigated over $10^1 \leq Ra \leq 10^6$ at $\varepsilon = 0.3$ for three different geometries (square cavity and skew cavity with $\delta = 30^\circ$ and $\delta = 150^\circ$) in Figure 11. Similar to previous section, results are plotted for the LMS approximation as reference solution in Figure 11(A),(B) and the difference of compressible and incompressible approximations are plotted in Figure 11(C)–(F). Comparing results in Figure 11(A), (B) indicate that, the growth rate of $S_{\psi,\,tot}$ is much faster than $S_{\Theta,\,tot}$. Indeed, the magnitude of $S_{\Theta,\,tot}$ for $Ra \leq 10^3$ is at least two order larger than $S_{\psi,\,tot}$. This means for all geometries at least up to $Ra = 10^3$, most of the irreversibility is due to heat transfer. For $Ra \geq 10^4$ the growth rate of $S_{\Theta,\,tot}$ versus Rayleigh number remains almost constant (linear growth rate) while $S_{\psi,\,tot}$ shows an exponential growth rate. Larger magnitude of $S_{\psi,\,tot}$ compared to the $S_{\Theta,\,tot}$ for $Ra \geq 10^4$ indicates that most of the irreversibilities at this range of the Rayleigh number is due to fluid friction. Comparing heat transfer and fluid friction irreversibilities of the compressible and incompressible approaches shows a negligible difference for $S_{\Theta,\,tot}$ for both incompressible approximations in Figure 11(C), (E) across the investigated range of the Rayleigh number while a clear mismatch is observable for $S_{\psi,\,tot}$ at $Ra \geq 10^5$ in Figure 11(D), (F). This mismatch may be attributed

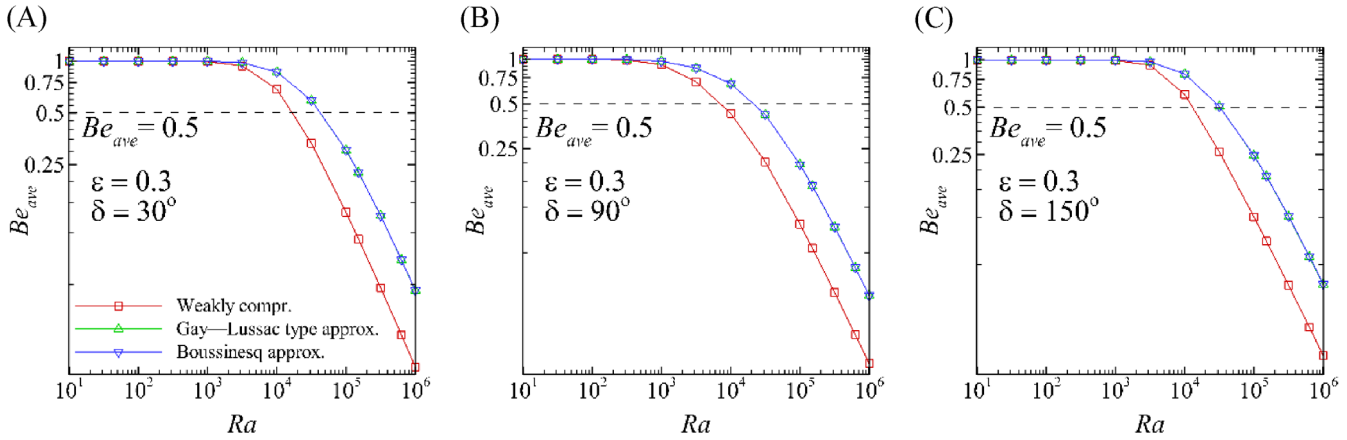

FIGURE 12 A plot of average Bejan number against Rayleigh number at $\varepsilon = 0.3$ in different geometries, (A) Right skew cavity ($\delta = 30^{\circ}$), (B) Square cavity, (C) Left skew cavity ($\delta = 150^{\circ}$) [Color figure can be viewed at wileyonlinelibrary.com]

to the divergence free flow field of incompressible approximation, which removes the last term of Equation (18). The difference of $S_{\Theta,\,\mathrm{tot}}$ and $S_{\psi,\,\mathrm{tot}}$ between the Boussinesq and Gay–Lussac-type approximations is also negligible in investigated range of Ra and ε. Finally, obtained results for $S_{\Theta,\,\mathrm{tot}}$ in different geometries plotted in Figures 11(A) show almost a similar trend for square and skew cavities with a sooner start of $S_{\Theta,\,\mathrm{tot}}$ growth versus Ra in square cavity. Results of $S_{\psi,\,\mathrm{tot}}$ in Figures 11(B) indicates skewing cavity causes delay to start of the exponential growth rate of this parameter, which is in agreement with later start of $\mathrm{Nu_{ave}}$ growth versus Ra for skew cavity compared to the square cavity in Figure 10.

Variations of the average Bejan number is investigated over $10^1 \leq \mathrm{Ra} \leq 10^6$ at $\varepsilon = 0.3$ for three different geometries in Figure 12. As seen, by increasing the Rayleigh number, the average Bejan number is decreased. This is because by increasing the Rayleigh number, thermal convection increasingly becomes the dominant mechanism driving the flow. The interesting feature of the average Bejan number is its transition to a value lower than 0.5 which indicates transition of dominant heat transfer mechanism from conduction to convection. Obtained average Bejan number in square cavity (Figure 12(B)) at $\mathrm{Ra} = 10^4$ under the LMS approximation shows a value less than 0.5, while incompressible approximations are showing values larger than 0.5 which means when temperature differences are large enough, the real heat transfer mechanism is convection dominated while incompressible approaches are approximating that as a conduction dominated regime. For skew cavities, this is occurring at higher Rayleigh number. In other words, incompressible approaches show a delay in predicting convection dominated regime at large temperature differences as the difference of the average Bejan number under different approximations becomes less in high Rayleigh numbers. As seen in Figure 12, $\mathrm{Be_{ave}}$ values versus Ra, start to deviate between compressible and incompressible approaches at $\mathrm{Ra} = 10^3$ for all geometries. Finally, similar to the average Nusselt number, both incompressible approximations are showing almost identical results for average Bejan number across investigated ranges of ε and Ra.

4.4 | Coefficient friction

Local coefficient friction along the isothermal walls is investigated for square and skew cavities ($\delta = 30^{\circ}$ and 150°) at $\mathrm{Ra} = 10^6$, $\varepsilon = 0.15$ and $\varepsilon = 0.3$ under different approximations in Figure 13. Results are showing a considerable mismatch between the weakly compressible approach and incompressible approximations. A comparison among C_f results at $\varepsilon = 0.15$ (Figure 13(A), (C), and (E)) and $\varepsilon = 0.3$ (Figure 13(B), (D) and (F)) reveals that this discrepancy augments by increasing the relative temperature differences. Indeed, by increasing the relative temperature difference, incompressible approximations show more deviations from the compressible approach. Presented results in Figure 13 indicate that extending the density variations to the advection term does not impose a significant impact on the local coefficient friction as C_f results of incompressible approximations are attached together in most of the regions. For the square cavity (Figure 13(C), (D)), the Gay–Lussac-type approximation is predicting slightly more accurate distribution of C_f with a visible difference around the maximum location of this parameter along the right wall at around $S \cong 0.3$ while the Boussinesq

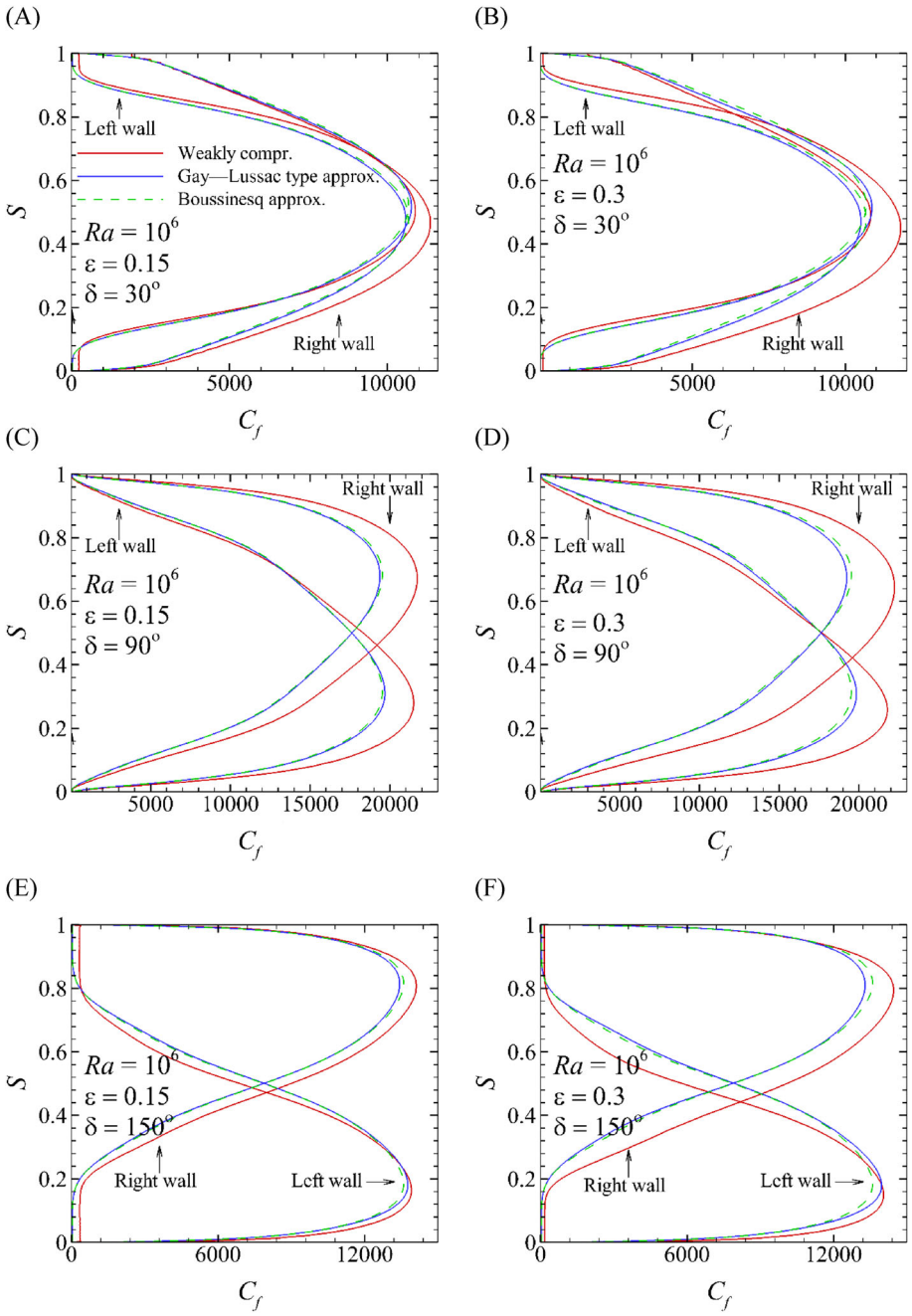

FIGURE 13 Local coefficient friction distributions along the isotherm walls at Ra = 10^6, $\varepsilon = 0.15$, and $\varepsilon = 0.3$ as stated, (A, B) Square cavity, (C, D) Right skew cavity ($\delta = 30^\circ$), (E, F) Left skew cavity ($\delta = 150^\circ$) [Color figure can be viewed at wileyonlinelibrary.com]

approximation is showing slightly more accurate distribution of C_f around the maximum location of this parameter along the left wall at around $S \cong 0.7$. This scenario is also valid for both of the right (Figure 13(A),(B)) and left (Figure 13(E),(F)) skew cavities with different locations of maximum differences.

Local coefficient friction along the horizontal adiabatic walls is also plotted for mentioned geometries at Ra = 10^6, $\varepsilon = 0.15$ and $\varepsilon = 0.3$ under different approximations in Figure 14. X_T and X_B in Figure 14(C)–(F) refer to the top and bottom horizontal adiabatic walls of the skew cavity, respectively. Presented results in Figure 14 show more deviation between the Boussinesq and Gay–Lussac-type approximations both deviating from the weakly compressible approach. In square cavity (Figure 14(C) and (D)), Gay–Lussac-type approximation is giving more accurate C_f results along the bottom wall at around $X \cong 0.85$ while the Boussinesq approximation is giving closer results to LMS approximation along the top wall at around $X \cong 0.2$. In rest of the regions, C_f results of the Boussinesq approximation lays between LMS and Gay-Lussac type approximations which means it is working better than the Gay–Lussac-type approximation in this part. This behavior is more clear at $\varepsilon = 0.3$ compared to the $\varepsilon = 0.15$. C_f results of incompressible approaches for right skew cavity with $\delta = 30^\circ$ (Figure 14(A),(B)) do not show much difference at $\varepsilon = 0.15$ but superior prediction of the Gay-Lussac

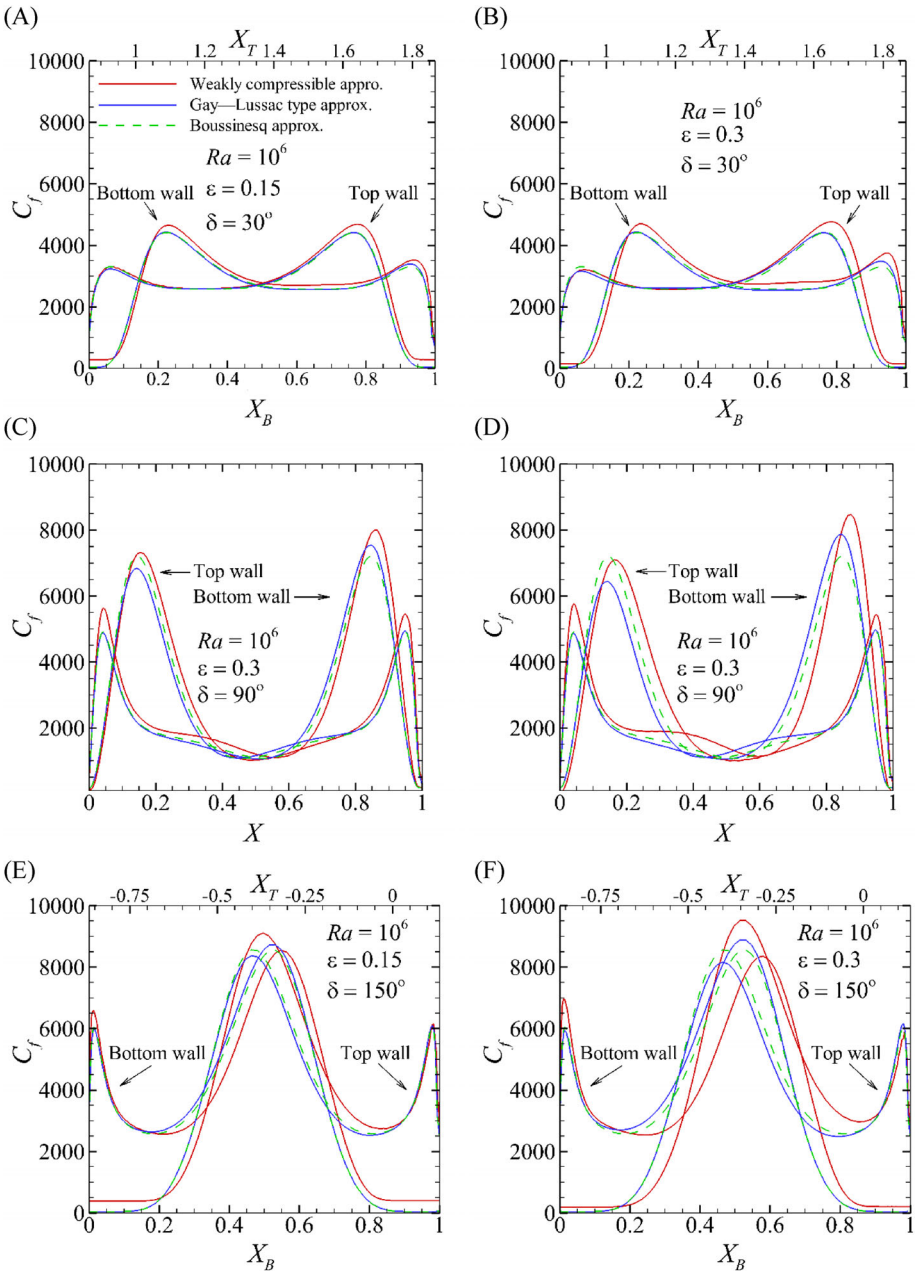

FIGURE 14 Local coefficient friction distributions along the horizontal adiabatic walls at Ra = 10^6, $\varepsilon = 0.15$, and $\varepsilon = 0.3$, (A, B), Square cavity, (C, D), Right skew cavity ($\delta = 30^{\circ}$), (E, F), Left skew cavity ($\delta = 150^{\circ}$) [Color figure can be viewed at wileyonlinelibrary.com]

type approximation in predicting maximum C_f at down-right region is clear. By increasing the relative temperature difference to 0.3, the difference of incompressible approximations becomes clear. Similar to the square cavity, C_f results of the Boussinesq approximation lays between two other approaches along the bottom wall but still superior prediction of C_f along the bottom wall at around $X_B \cong 0.95$ is valid. Increasing the relative temperature difference to 0.3 pushes the C_f results of the Gay-Lussac type approximation between two other approaches along the top wall in this geometry. Finally, for the left skew cavity with $\delta = 150^{\circ}$ (Figure 14(E),(F)), the difference of the C_f results along the horizontal adiabatic walls is clear between incompressible approximations for both of $\varepsilon = 0.15$ and 0.3. In this geometry, predicted C_f results along the top wall by the Gay-Lussac type approximations is more accurate up to $X_T \cong 0.4$ while after that Boussinesq approximation is showing closer results to the LMS approximation. In addition, predicted C_f results along the bottom wall by the Gay-Lussac type approximations is more accurate up to $X_B \cong 0.2$ while after that Boussinesq approximation is working better up to $X_B \cong 0.6$ where the Gay–Lussac-type approximation recovers its greater performance after that up to $X_B \cong 0.65$. For $X_B > 0.65$, C_f values of incompressible approximations are attached and they show almost no difference.

4.5 | Computational cost and convergence rate analysis

In this section, the advantage of solving equation in secondary variables form is discussed in the context of the computational cost and convergence rate. Whole of the numerical solution procedure using second-order Adams–Bashforth/Crank–Nicolson temporal scheme may be summarized in five successive steps through Equations (29)–(33) that is explained in brief in Section 3:

$$\psi^{n+1} = -[\mathrm{D}]^{-1} \times \omega^n. \tag{34}$$

$$\omega^* = \omega^n + \Delta t \left(-\frac{3}{2}(1 - 2\varepsilon\overline{\overline{\Theta^n}}) \underbrace{N(\omega^n)}_{\frac{\text{Central}}{\text{Upwind}}} + \frac{1}{2}(1 - 2\varepsilon\overline{\overline{\Theta^{n-1}}}) \underbrace{N(\omega^{n-1})}_{\frac{\text{Central}}{\text{Upwind}}} + (\mathrm{Pr}/2) \underbrace{\mathrm{D}(\omega^n)}_{\text{Central}} + \mathrm{Ra.\,Pr}\,.\overline{\overline{(\partial\Theta/\partial X)^n}} \right). \tag{35}$$

$$\omega^{n+1} = -[(\mathrm{Pr}/2)\mathrm{D} - (1/\Delta t)I]^{-1} \times (1/\Delta t)\omega^*. \tag{36}$$

$$\Theta^* = \Theta^n + \Delta t \left(-\frac{3}{2} \underbrace{N(\Theta^n)}_{\text{Central/Upwind}} + \frac{1}{2} \underbrace{N(\Theta^{n-1})}_{\text{Central/Upwind}} + \frac{1}{2} \underbrace{D(\Theta^n)}_{\text{Central}} \right). \tag{37}$$

$$\Theta^{n+1} = -[(1/2)D - (1/\Delta t)I]^{-1} \times (1/\Delta t)\Theta^* \tag{38}$$

These equations regarding boundary conditions are solved in a loop until the maximum difference of scalar variables satisfy stop criteria which is defined in Section 3 as 10^{-7}. Among three equations in the secondary variables form, the stream function equation is the only linear equation (Poisson equation) which its solution in each iteration is straightforward. To make the solution procedure as fast as possible, inverse matrix of Laplacian operator ($[D]^{-1}$) with a zero Dirichlet boundary condition for stream-function along the walls of the cavity is constructed by CVFEM solver and it is multiplied by the vorticity vector in each iteration to update stream function field. For two other nonlinear equations, that is, vorticity and energy equations, two possible scenarios are considered in which, the nonlinear advection and convection terms are discretized via upwind or central schemes. This is a benefit of solving governing equations in secondary variables form to approximate the nonlinear terms in vorticity and energy equations by central scheme even for convection-dominated regimes. In other words, applying central scheme for primitive variables at convection-advection dominated regimes will lead to diverging solution procedure. The diffusion terms due to their elliptical nature are discretized using central scheme. In addition, temperature prefactor, that is, $(1 - 2\varepsilon\Theta)$ and source term of vorticity equation (which are shown by an overbar) are lagged from the current and last update of the temperature fields. Similar to the stream function equation, an inverse Laplacian matrix is constructed for correction steps of the vorticity and energy equations, that is, Equations (31) and (33) to accelerate the solution procedure.

For comparison purposes, required computational time and convergence rate is shown in Figure 15 for square cavity at $\mathrm{Ra} = 10^2$ and $\varepsilon = 0.3$ for a mesh file having 10 k elements. This Rayleigh number lays in conduction dominated regime and it is possible to apply both upwind and central schemes for nonlinear terms of the governing equations in primitive variables. Another reason to pick this low Rayleigh number is obtaining the minimum computational time due to applying different approaches since required iterations (and consequently computational time) is increased by increasing the Rayleigh number. CPU-time of submitted jobs for all cases are measured by Monash University super-computer facilities (MonARCH). Obtained CPU-time show a 8.5% less and a 3.4% more computational cost for central and second-order-upwind schemes, respectively, when governing equations are solved via secondary variables rather than primitive variables. It should be noted that two momentum equations in secondary variable form are merged to one vorticity equation. In other words, in secondary variables form, one less equation is solved. As mentioned earlier, this is the *minimum* difference as required iterations and consequently computational time increases at higher Rayleigh numbers. In Figure 15(A), required CPU-time for upwind scheme is considerably more than central scheme. This is due to higher computational cost of determining flow direction and nodes located at upstream to approximate fluxes at each integration point. Presented data in Figure 15(A) suggests that upwind scheme is not suitable/recommended for the numerical solution of the governing equations in secondary variables form.

Convergence rates of the different schemes are compared in Figures 15(B)–(F) for different schemes in both secondary and primitive variables. Obtained results indicate that primitive variables in both cases (upwind and central schemes)

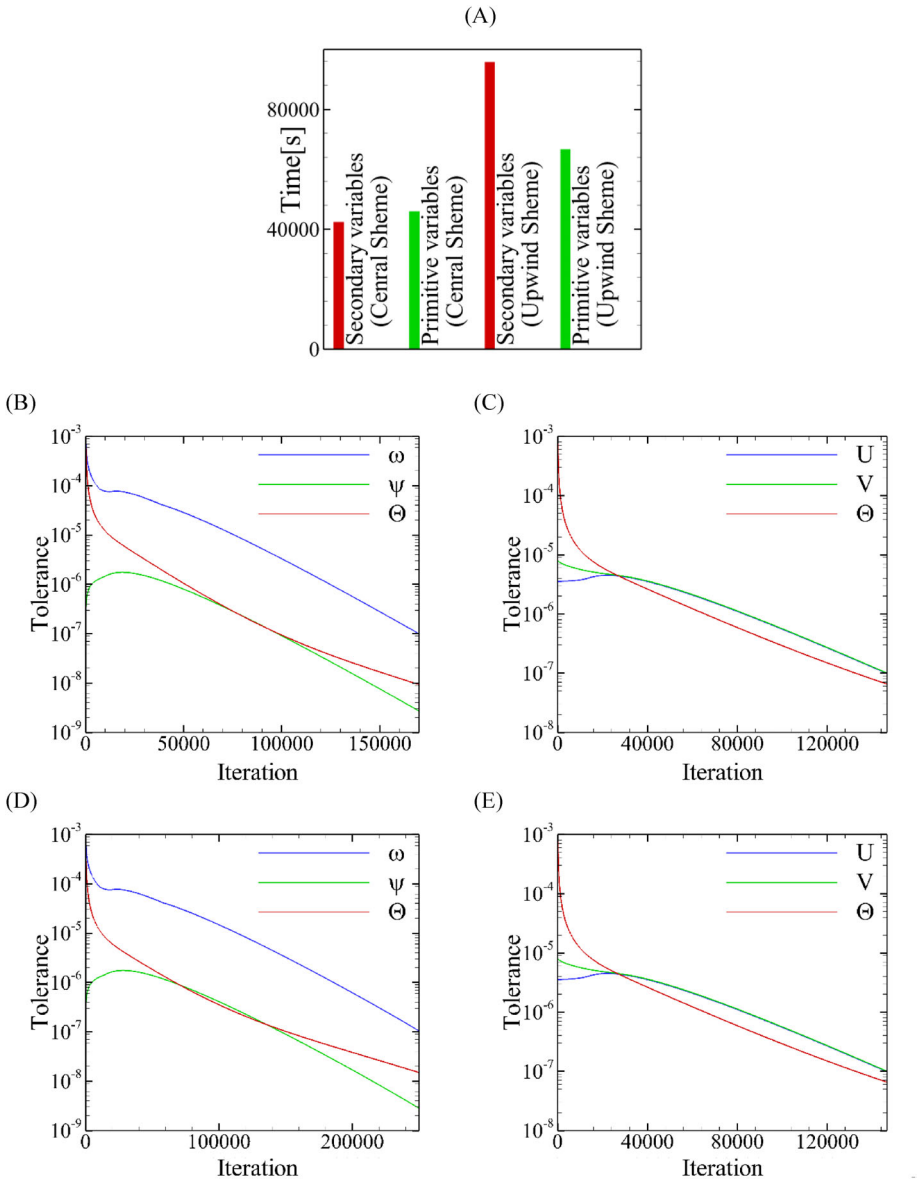

FIGURE 15 Computational cost and convergence rate of the computations for square cavity at $Ra = 10^2$ and $\varepsilon = 0.3$ using primitive and secondary variables, (A) CPU-time, (B) convergence rate of the secondary variables; central scheme, (C) convergence rate of the primitive variables; central scheme, (D) convergence rate of secondary variables; second-order upwind, (E) convergence rate of the primitive variables; second-order upwind. For all cases, a global time-step of 10^{-6} ($dt = 10^{-6}$) is used for calculations [Color figure can be viewed at wileyonlinelibrary.com]

have faster convergence rate but lower computational cost of secondary variables causes the solution procedure to be finalized before than primitive variables.

5 | CONCLUSION

In this paper, a new secondary-variable formulation for natural convection is applied to the square and skew cavity benchmark problems up to $Ra = 10^6$ and $\varepsilon = 0.3$ at $Pr = 6.14$. The formulation is derived based on considering density variations in the advection term of the momentum equations in addition to the gravity term, offering an improved description of convection in rapidly rotating regions of the flow. A Froude number proportional to the relative temperature difference is derived describing the deviation from the Boussinesq approximation. It is also shown that the Gay–Lussac parameter (also relating to deviation from the Boussinesq approximation) may be expressed by an equivalent relative temperature difference. Comparing stream-function fields for a physically meaningful range of the relative temperature difference versus both a weakly compressible approach and the Boussinesq approximation indicates that the new formulation gives consistent and slightly superior flow-related data. Results obtained for local Nusselt number distribution from the proposed formulation shows that the Gay–Lussac-type approximations still require modifications to yield accurate results comparable to the compressible approach. However, for considered problems in this study, a reversal of the local Nusselt

number distributions along the two isothermal walls nullifies the mismatch of the average Nusselt number between the compressible and incompressible solutions. An entropy generation analysis indicates that both of the Boussinesq and Gay–Lussac-type approximations show a considerable mismatch of Bejan number at middle Rayleigh number and high relative temperature differences. However, this mismatch becomes less at high Rayleigh numbers. Comparing coefficient friction results of the weakly compressible and incompressible approximations at high-relative temperature differences indicate that extending the density variations to the advection terms does not significantly increase the quality of flow field in all regions compared to the Boussinesq approximation. Finally, a computational cost analysis indicates that primitive variables have faster convergence rate but applying a central scheme for nonlinear terms and one less equation in the secondary variable form leads to the less computational cost.

ACKNOWLEDGEMENTS

This research was supported by the Australian Research Council through Discovery Projects DP150102920 and DP180102647. Peyman Mayeli is supported by a Monash Graduate Scholarship and a Monash International Postgraduate Research Scholarship. The authors are also supported by time allocations on the National Computational Infrastructure (NCI) peak facility and the Pawsey Supercomputing Centre through NCMAS grants. NCI is supported by the Australian Government.

NOMENCLATURE

B	buoyancy term
$\mathrm{Be}_{\mathrm{ave}}$	average Bejan number
c_f	skin friction coefficient
D	diffusion operator
e_g	unit vector in gravity direction
Fr	Froude number
g	gravitational acceleration
Ga	Gay–Lussac number ($\beta\Delta\theta$)
L_{ref}	reference length
$\mathrm{Nu}_{\mathrm{ave}}$	average Nusselt number
$\mathrm{Nu}_{\mathrm{loc}}$	local Nusselt number
p	pressure
p^*	modified pressure
P	dimensionless pressure
P_{th}	thermodynamic pressure
Pr	Prandtl number
R	ideal gas constant
Ra	Rayleigh number
S	surface
S_Θ	entropy generation due to heat transfer
S_ψ	entropy generation due to fluid friction
T	temperature
$\boldsymbol{x}$	coordinate vector
$\boldsymbol{X}$	dimensionless coordinate vector
$\boldsymbol{u}$	velocity vector
$\boldsymbol{U}$	dimensionless velocity vector
α	thermal diffusivity
β	isobaric expansion coefficient
δ	angle of skew cavity
ε	relative temperature difference
θ	physical temperature
Θ	dimensionless temperature
μ	dynamic viscosity
ν	kinematic viscosity
ρ	density

ρ_0 reference density
τ_w wall shear stress
ϕ gravitational potential
χ irreversibility distribution ratio
ψ stream-function
ω vorticity

SUBSCRIPT

ave average
c cool
h hot
loc local
ref reference
tot total

SUPERSCRIPT

n current time-step
$n-1$ previous time-step
$-$ refers to a lagged value

DATA AVAILABILITY STATEMENT

Data sharing is not applicable to this article as no new data were created in this study.

ORCID

Peyman Mayeli https://orcid.org/0000-0003-4084-2627

REFERENCES

1. Boussinesq J. *Theorie Analytique de la Chaleur*. Vol II. Paris: Gauthier-Villars; 1903.
2. de Vahl Davis G. Natural convection of air in a square cavity, a benchmark numerical solution. *Int J Numer Methods Fluids*. 1983;3:249-264. https://doi.org/10.1002/fld.1650030305.
3. Lage JL, Bejan A. The Ra-Pr domain of laminar convection in an enclosure heated from the side. *Numer Heat Transf A*. 1991;19:21-41. https://doi.org/10.1080/10407789108944836.
4. Mohamad A, Sheremet MA, Taler J, Ocłoń P. Natural convection in differentially heated enclosures subjected to variable temperature boundaries. *Int J Numer Methods Heat Fluid Flow*. 2019;29(11):4130-4141. https://doi.org/10.1108/HFF-02-2019-0137.
5. Shermet M, Groson T, Pop I. MHD free convection flow in an inclined square cavity filled with both nanofluids and gyrotactic microorganisms. *Int J Numer Methods Heat Fluid Flow*. 2019;29(12):4642-4659. https://doi.org/10.1108/HFF-03-2019-0264.
6. Wan DC, Patnail BSV, Wei GW. A new benchmark quality solution for the buoyancy-driven cavity by discrete singular convolution. *Numer Heat Transf B*. 2001;40:199-228. https://doi.org/10.1080/104077901752379620.
7. Ashrafizadeh A, Nikfar M. On the numerical solution of generalized convection heat transfer problems via the method of proper closure equations–Part II: application to test problems. *Numer Heat Transf B*. 2016;70(2):204-222. https://doi.org/10.1080/10407782.2016.1173467.
8. Bondareva NS, Sheremet MA, Oztop HF, Abu-Hamdeh N. Free convection in an open triangular cavity filled with a nanofluid under the effects of Brownian diffusion. thermophoresis and local heater. *J Heat Transf T ASME*. 2018;140(4):042502. https://doi.org/10.1115/1.4038192.
9. Varol Y, Koca A, Oztop HF. Natural convection in a triangle enclosure with flush mounted heater on the wall. *Int Comm Heat Mass Transf*. 2006;33(8):951-958. https://doi.org/10.1016/j.icheatmasstransfer.2006.05.003.
10. Rahman MM, Alam MS, Al-Salti N, Eltayeb IA. Hydromagnetic natural convective heat transfer flow in an isosceles triangular cavity filled with nanofluid using two-component nonhomogeneous model. *Int J Therm Sci*. 2016;107:272-288. https://doi.org/10.1016/j.ijthermalsci.2016.04.009.
11. Bhowmick S, Xu F, Zhang X, Saha SC. Natural convection and heat transfer in a valley shaped cavity filled with initially stratified water. *Int J Therm Sci*. 2018;128:59-69. https://doi.org/10.1016/j.ijthermalsci.2018.02.019.
12. Wu YL, Liu GR, Gu YT. Application of meshless local Petrov-Galerkin (MLPG) approach to simulation of incompressible flow. *Numer Heat Transf B*. 2005;48(5):459-475. https://doi.org/10.1080/10407790500324763.
13. Abu-Nada E, Masoud Z, Hijazi A. Natural convection heat transfer enhancement in horizontal concentric annuli using nanofluids. *Int Comm Heat Mass Transf*. 2008;35:657-665. https://doi.org/10.1016/j.icheatmasstransfer.2007.11.004.
14. Ashorynejad HR, Mohamad AA, Sheikholeslami M. Magnetic field effects on natural convection flow of a nanofluid in a horizontal cylindrical annulus using lattice Boltzmann method. *Int J Therm Sci*. 2013;64:240-250. https://doi.org/10.1016/j.ijthermalsci.2012.08.006.

15. Paillere H, Viozat C, Kumbaro A, Toumi I. Comparison of low mach number models for natural convection problems. *Heat Mass Transf*. 2000;36:567-573. https://doi.org/10.1007/s002310000116.
16. Szewc K, Pozorski J, Tanière A. Modelling of natural convection with smoothed particle hydrodynamics: non-Boussinesq formulation. *Int J Heat Mass Transf*. 2011;54:4807-4816. https://doi.org/10.1016/j.ijheatmasstransfer.2011.06.034.
17. Niajalili H, Mayeli P, Naghashzadegan M, Poshtiri AH. Techno-economic feasibility of off-grid solar irrigation for a rice paddy in Guilan province in Iran: a case study. *Sol Energy*. 2017;150:456-557. https://doi.org/10.1016/j.solener.2017.05.012.
18. Vierendeels J, Merci B, Dick E. Numerical study of natural convective heat transfer with large temperature differences. *In J Numer Methods Heat Fluid Flow*. 2001;11(4):329-341. https://doi.org/10.1108/09615530110389117.
19. Fu W, Li C, Huang C, Huang J. An investigation of a high temperature difference natural convection in a finite length channel without Bossinesq assumption. *Int J Heat Mass Transf*. 2009;52:2571-2580. https://doi.org/10.1016/j.ijheatmasstransfer.2009.01.012.
20. S. Busto, M. Tavelli, W. Boscheri, M. Dumbser, Efficient high order accurate staggered semi-implicit discontinuous Galerkin methods for natural convection problems. *Comput Fluids*. 2020;198:104399. https://doi.org/10.1016/j.compfluid.2019.104399.
21. Bermúdez A, Busto S, Dumbser M, Ferrín JL, Saavedra L, Vázquez-Cendón ME. A staggered semi-implicit hybrid FV/FE projection method for weakly compressible flows. *J Comput Phy*. 2020;421:109743. https://doi.org/10.1016/j.jcp.2020.109743.
22. Paolucci S. *On the Filtering of Sound from the Navier-Stokes Equations, Technical Report SAND 82–8257*. Vol 9. Livermore, CA: Sandia National Laboratories; 1982.
23. Vierendeels J, Merci B, Dick E. A multigrid method for natural convective heat transfer with large temperature differences. *J Comput Appl Math*. 2004;168(1–2):509-517. https://doi.org/10.1016/j.cam.2003.08.081.
24. Becker R, Braack M. Solution of a stationary benchmark problem for natural convection with large temperature difference. *Int J Therm Sci*. 2002;41(5):428-439. https://doi.org/10.1016/S1290-0729(02)01335-2.
25. Pesso T, Piva S. Laminar natural convection in a square cavity: low Prandtl numbers and large density differences. *Int J Heat Mass Transf*. 2009;52(3–4):1036-1043. https://doi.org/10.1016/j.ijheatmasstransfer.2008.07.005.
26. Lopez JM, Marques F, Avila M. The Boussinesq approximation in rapidly rotating flows. *J Fluid Mech*. 2013;737:56-77. https://doi.org/10.1017/jfm.2013.558.
27. Mayeli P, Sheard G. A new formulation for Boussinesq-type natural convection flows applied to the annulus cavity problem. *Int J Numer Methods Fluids*. 2020;93(3):683-702. https://doi.org/10.1002/fld.4904.
28. Osorio A, Avila R, Cervantes J. On the natural convection of water near its density inversion in an inclined square cavity. *Int J Heat Mass Transf*. 2004;47(19–20):4491-4495. https://doi.org/10.1016/j.ijheatmasstransfer.2004.06.003.
29. Souza M, Miranda R, Machado H. Natural convection in enclosures with variable fluid properties. *Int J Numer Methods Heat Fluid Flow*. 2003;13(8):1079-1096. https://doi.org/10.1108/09615530310501966.
30. Chenoweth DR, Paolucci S. Natural convection in an enclosed vertical air layer with large horizontal temperature differences. *JFM*. 1986;169:173-210. https://doi.org/10.1017/S0022112086000587.
31. Basak T, Kaluri RS, Balakrishnan AR. Effects of thermal boundary conditions on entropy generation during natural convection. *Numer Heat Transf A*. 2011;59(5):372-402. https://doi.org/10.1080/10407782.2011.549075.
32. Ilis GG, Mobedi M, Sunden B. Effect of aspect ratio on entropy generation in a rectangular cavity with differentially heated vertical walls. *Int Comm Heat Mass Transf*. 2008;35(6):696-703. https://doi.org/10.1016/j.icheatmasstransfer.2008.02.002.
33. Nayak RK, Bhattacharyya S, Pop I. Heat transfer and entropy generation in mixed convection of a nanofluid within an inclined skewed cavity. *Int Comm Heat Mass Transf*. 2016;102:596-609. https://doi.org/10.1016/j.ijheatmasstransfer.2016.06.049.
34. Bondareva NS, Sheremet MA, Oztop HF, Abu-Hamdeh N. Entropy generation due to natural convection of a nanofluid in a partially open triangular cavity. *Adv Powder Technol*. 2017;28:244-255. https://doi.org/10.1016/j.apt.2016.09.030.
35. Sheremet MA, Pop I, Oztop HF, Abu-Hamdeh N. Natural convection of nanofluid inside a wavy cavity with a non-uniform heating: entropy generation analysis. *In J Numer Methods Heat Fluid Flow*. 2017;27:958-980. https://doi.org/10.1108/HFF-02-2016-0063.
36. Astanina MS, Sheremet MA, Oztop HF, Abu-Hamdeh N. MHD natural convection and entropy generation of ferrofluid in an open trapezoidal cavity partially filled with a porous medium. *Int J Mech Sci*. 2018;136:493-502. https://doi.org/10.1016/j.ijmecsci.2018.01.001.
37. Mayeli P, Nili-Ahmadabadi M, Pirzadeh MR, Rahmani P. Determination of desired geometry by a novel extension of ball spine algorithm inverse method to conjugate heat transfer problems. *Comput Fluids*. 2017;154:390-406. https://doi.org/10.1016/j.compfluid.2016.05.022.
38. Hesami H, Mayeli P. Development of the ball-spine algorithm for the shape optimization of ducts containing nanofluid. *Numer Heat Transf A*. 2016;70(12):1371-1389. https://doi.org/10.1080/10407782.2016.1243976.
39. Nikfar M, Mayeli P. Surface shape design in different convection heat transfer problems via a novel coupled algorithm. *J Heat Transf-Trans ASME*. 2018;140(2):021702-1-021702-15. https://doi.org/10.1115/1.4037581.
40. Mayeli P, Hesami H, Moghaddam MHDF. Numerical investigation of the MHD forced convection and entropy generation in a straight duct with sinusoidal walls containing water-Al2O3 nanofluid. *Numer Heat Transf A*. 2017;71(12):1371-1389. https://doi.org/10.1080/10407782.2016.1243976.
41. Mayeli P, Hesami H, Besharati-Foumani H, Niajalili M. Al_2O_3-water nanofluid heat transfer and entropy generation in a ribbed channel with wavy wall in the presence of magnetic field. *Numer Heat Transf A*. 2018;73(9):604-623. https://doi.org/10.1080/10407782.2018.1461494.
42. Ashrafizadeh A, Alinia B, Mayeli P. A new co-located pressure-based discretization method for the numerical solution of incompressible Navier-stokes equations. *Numer Heat Transf B*. 2015;67(6):563-589. https://doi.org/10.1080/10407790.2014.992094.
43. Mayeli P, Nikfar M. Temperature identification of a heat source in conjugate heat transfer problems via an inverse analysis. *Int J Numer Methods Heat Fluid Flow*. 2019;29(10):3994-4010. https://doi.org/10.1108/HFF-05-2018-0193.

44. Nikfar M, Ashrafizadeh A, Mayeli P. Inverse shape design via a new physical-based iterative solution strategy. *Inverse Probl Eng*. 2015;23(7):1138-1162. https://doi.org/10.1080/17415977.2014.973873.
45. Mayeli P, Sheard G. Studying the natural convection problem in a square cavity by a new vorticity-stream-function approach. Paper presented at: Proceedings of the 22nd Australasian Fluid Mechanics Conference; December 7–10, 2020; The University of Queensland, Brisbane, Australia. https://doi.org/10.14264/b2c1622
46. Le Quéré P, Weisman C, Paillère H, et al. Modelling of natural convection flows with large temperature differences: a benchmark problem for low mach number solvers Part 1 reference solutions. *ESAIM Math Modell Numer Anal*. 2005;39(3):609-616. https://doi.org/10.1051/m2an:2005027.

How to cite this article: Mayeli P, Sheard GJ. Natural convection and entropy generation in square and skew cavities due to large temperature differences: A Gay–Lussac-type vorticity stream-function approach. *Int J Numer Meth Fluids*. 2021;1–25. https://doi.org/10.1002/fld.4980